



HAL
open science

Influence of an Oriented External Electric Field on the Mechanism of Double Proton Transfer between Pyrazole and Guanidine: from an Asynchronous Plateau Transition State to a Synchronous or Stepwise Mechanism

Antoine Geoffroy-Neveux, Vanessa Labet, M. Esmail Alikhani

► To cite this version:

Antoine Geoffroy-Neveux, Vanessa Labet, M. Esmail Alikhani. Influence of an Oriented External Electric Field on the Mechanism of Double Proton Transfer between Pyrazole and Guanidine: from an Asynchronous Plateau Transition State to a Synchronous or Stepwise Mechanism. *Journal of Physical Chemistry A*, 2022, 126 (20), pp.3057-3071. 10.1021/acs.jpca.1c10553 . hal-03695204

HAL Id: hal-03695204

<https://hal.sorbonne-universite.fr/hal-03695204>

Submitted on 15 Nov 2022

HAL is a multi-disciplinary open access archive for the deposit and dissemination of scientific research documents, whether they are published or not. The documents may come from teaching and research institutions in France or abroad, or from public or private research centers.

L'archive ouverte pluridisciplinaire **HAL**, est destinée au dépôt et à la diffusion de documents scientifiques de niveau recherche, publiés ou non, émanant des établissements d'enseignement et de recherche français ou étrangers, des laboratoires publics ou privés.

1
2
3
4 Influence of an Oriented External Electric Field on the Mechanism of Double Proton-
5 Transfer between Pyrazole and Guanidine: from an Asynchronous Plateau Transition
6 State to a Synchronous or Stepwise Mechanism
7
8
9

10
11
12
13 Antoine Geoffroy-Neveux, Vanessa Labet, and M. Esmail Alikhani*

14
15 MONARIS UMR 8233 CNRS, Sorbonne Université, 4 place Jussieu, 75252 Paris Cedex 05, France
16
17

18
19 **Abstract**
20

21
22 The double proton transfer (DPT) reaction between pyrazole and guanidine, a concerted reaction but
23 strongly asynchronous and presenting a “plateau transition region”, has been theoretically
24 reinvestigated in the presence of an external uniform electric field. First, we computed the reaction
25 path by DFT and proposed a very detailed description of the constitutive electronic events, based on
26 the ELF topology and the bond evolution theory. Then, we studied the effect of an oriented external
27 electric field (OEEF) on the reaction mechanism, for an OEEF oriented along the proton transfer axis. We
28 observe that in one direction, the DPT reaction can be transformed into a stepwise reaction, going through a
29 stabilized single proton transferred intermediate. Contrarily, the two proton transfers occur simultaneously
30 when the electric field is applied in the opposite direction. In the latter case, the order in which the two
31 protons are transferred in the same elementary step can even be reversed if the OEEF is intense enough.
32 Finally, it has been shown that the evolution of the double proton transfer reaction in the presence of an
33 electric field could be quantitatively anticipated by analysing the ELF value at the bifurcation point between
34 $V(A, H)$ proton donor and $V(B)$ proton acceptor of the double hydrogen bonded complex in the
35 entrance channel.
36
37
38
39
40
41
42
43
44
45
46
47
48
49
50
51
52
53
54
55

56
57
58 * Corresponding author : esmail.alikhani@sorbonne-universite.fr
59
60

Introduction

The effect of an electric field on molecular structure and chemical reactivity has long been known. At a very fundamental level, electric fields have been used in numerical experiments to model environmental effects (solid state, solution)¹⁻⁵ or specific experimental conditions (e.g. STM⁶) and thus better understand their influence on molecular structure as well as on other observables measured by various experimental techniques (e.g. NMR^{7,8}, vibrational spectroscopy⁹⁻¹¹). Thanks to these studies, the effect of an electric field on covalent¹² and non-covalent^{8,13-16} bonds has been largely elucidated. Hydrogen bonded complexes^{7,17-20} and proton transfer reactions^{4,21-23} in particular have been widely investigated, due to their widespread occurrence in chemistry and biology. Thus, it could for example be evidenced that an external electric field can drive proton transfer between two partners in cases for which the reaction does not occur in the gas phase.²³

Besides, in a more applied domain, it is now well established that electrostatic interactions play a major role in enzyme catalysis.²⁴ And since its original formulation by Warshel some time ago,²⁵ tremendous work has been performed to take advantage of the enzyme active site preorganization idea, combining the development of experimental techniques,²⁶⁻²⁸ complemented with numerical experiments,²⁹ to measure and analyse electric fields inside enzyme active sites and the use of computational modelling to design optimal electric fields and synthetic enzymes.³⁰⁻³²

However, it was not until quite recently, with the experiment by Aragonès et al.,³³ that oriented external electric fields (OEEF) were actually considered as “*smart reagents*”,³⁴ i.e. as viable means to catalyse a chemical reaction on purpose in non-biological systems.^{34,35} Since then, the development of experimental devices that harness electric field induced catalysis has been a major objective.³⁶⁻³⁸

Some years ago, Shaik initiated rationalisation of the OEEF effect on chemical reactivity,^{39,40} using the valence-bond (VB) diagram model of chemical reactivity.^{41,42} This work was pursued more intensively⁴³⁻⁴⁸ after the experiment of Aragonès et al.,³³ leading to the formulation of the so-called “reaction-axis rule”.³⁴ This rule states that if an OEEF is applied along the direction in which electrons are transferred during a chemical reaction (reaction-axis) then the reaction can be catalysed or inhibited by the field depending on its orientation. Furthermore, when 2 products can be formed, the application of an electric field along the reaction axis³⁹ or another direction⁴⁰ can also modify the reaction selectivity. It requires that this direction leads to very different dipole moment variations

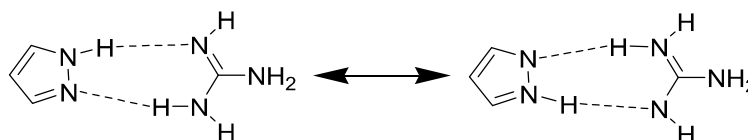
1
2
3 between the reactive complex and the transition state depending on which of both approach
4 geometries leading to the products is considered.
5
6

7
8 Let us go back to the reaction-axis rule. The origin of this phenomenon lies in the greater
9 polarizability of transition states (TS) with respect to that of reactants and/or products. In the VB
10 framework, it implies that in the TS structure, there is a greater contribution of ionic and/or charge
11 transfer (CT) structures (stronger mixing with covalent structures) than in the reactant and product.
12 These ionic / CT structures are characterised by a dipole moment oriented according to the electronic
13 transfer taking place during the reaction (reaction axis). Under the effect of an [electric field](#), these
14 ionic / CT structures are all the more stabilised / destabilised as the corresponding dipole moments
15 are oriented according to the electric field (stabilisation in one direction / destabilisation in the other
16 one).^{24,25,28,30,43,44} At sufficiently high field strengths, this can even lead to such a strong stabilisation
17 that a zwitterionic reaction intermediate appears along the reaction coordinate.⁴⁰ It is therefore
18 theoretically possible to switch from a concerted mechanism to a stepwise reaction under the effect
19 of an electric field. This is of course reflected in a change in the height of the reaction activation
20 barrier, but also and above all in a change in the reaction coordinate. Indeed, we go from a reaction
21 for which several processes occur simultaneously (concerted mechanism) to a reaction for which
22 these same processes occur successively (stepwise mechanism). It is precisely this mechanistic
23 crossover that we wish to examine in greater detail in this study. Indeed, switching from a concerted
24 mechanism to a stepwise reaction or vice versa has a potential effect on the stereoselectivity of a
25 reaction, which can be particularly interesting in synthetic chemistry.
26
27
28
29
30
31
32
33
34
35
36
37
38
39

40 To explore this idea, we chose double [intermolecular](#) proton transfer (DPT) as a [model reaction](#).
41 Indeed, most of these reactions can be seen as the motion of two positively charged particles in
42 opposite directions. Therefore, an OEEF oriented along the transfer direction is likely to have
43 opposite effects on each of both proton transfers, one being facilitated, the other inhibited. More
44 precisely, some years ago, exploring again an observation made by Politzer *et al.* on a ring opening
45 reaction,^{49,50} Rauhut *et al.*⁵¹ identified a peculiar class of DPT reactions exhibiting unusual potential
46 energy profiles along the reaction coordinate, very flat in the transition state region. These were
47 called “*plateau reactions*” and the reason for the plateau was attributed to the fact that these reactions
48 were at the transition between concerted and stepwise mechanisms. To gain insight on the physical
49 meaning of such plateaus on the potential energy surface, Rauhut *et al.* extensively studied these
50 DPT reactions^{52–54} in static studies by various computational methods, some of them taking account
51 for quantum effects (ZPE correction, proton tunnelling).⁵³ The plateau was shown to be sensitive to
52
53
54
55
56
57
58
59
60

1
2
3 the computational methodology used; nonetheless, its persistence in some of the cases investigated
4 suggests plateau reactions constitute a distinguish class of reactions, what was confirmed by quantum
5 dynamic studies.^{55,56} Recently, in a theoretical investigation of the Watson–Crick Guanine–Cytosine
6 base pair ⁵⁷ Arabi and Matta showed that the single imaginary vibrational frequency characterizing
7 the transition state decreases in absolute value from 1316.8i to 612.9i cm⁻¹, when the external field
8 strength increases from zero to 51.40 MV.cm⁻¹. They also found that the variation of the imaginary
9 vibrational frequency is accompanied by a flattening of the potential energy profile around the TS
10 structure. Therefore we believe that these plateau reactions are very likely to convert into true
11 concerted or true stepwise reactions under the action of an OEEF.
12
13
14
15
16
17
18

19 In this work we chose to focus on the plateau DPT reaction between pyrazole and guanidine that can
20 be schematized in Chart 1:
21
22
23



24
25
26
27
28
29
30 **Chart 1** Formal representation of the double proton transfer reaction in the pyrazole-guanidine system.

31
32 Our first objective will be to study the effect of an OEEF on this plateau reaction. Therefore, the
33 reaction mechanism will be explored under the influence of an OEEF oriented along the hydrogen
34 bonds, in both directions. To analyse the OEEF effect on the electronic events, we will follow in
35 details bond breaking / formation making use of the Electron Localization Function topology, in the
36 framework of the Bond Evolution Theory (BET). Note that though we are aware of the fact that
37 solvent can have an influence on the shape of the potential energy surface of DPT reactions,
38 transforming a transition state into a reaction intermediate,⁵⁸ this explanatory work will be carry out
39 in the gas phase. Pursuing the idea to use OEEF as smart reagents, we will also examine to what
40 extent our topological analysis can provide a quantitative index to predict the effect of an OEEF on
41 the synchronicity of a DPT reaction.
42
43
44
45
46
47
48
49

50 51 **Computational and theoretical details**

52 All first principle calculations were performed using the Gaussian 09 quantum chemical package.⁵⁹
53 Optimizations of the stationary points on the potential energy surface were obtained using the
54 ω B97X-D exchange-correlation functional^{60,61} which accounts for dispersion energy and long-range
55
56
57
58
59
60

1
2
3 interaction. The Pople's triple- ζ quality basis set extended with polarization and diffuse functions, 6-
4 311++G(2d,2p),^{62,63} has been used for all atoms.

5
6
7 Calculation of reaction path was performed by following the intrinsic-reaction-coordinate (IRC)⁶⁴
8 labeled as ξ and expressed in mass-weighted Cartesian coordinates which links the transition state
9 (characterized by a single imaginary frequency and labeled as TS) to the reactant (R) and product
10 (P). We note that in this work R and P stand for hydrogen-bonded complexes formed between two
11 molecular moieties in the entrance and exit channels of reaction, respectively.
12
13
14
15

16
17 All IRC calculations have been performed using local quadratic approximation (LQA) algorithm,^{65,66}
18 force constants computed only at the first point (CalcFC), and a step-size equal to 4 (StepSize = 4)
19 in units of $0.01 \text{ amu}^{1/2} \cdot \text{Bohr}$.
20
21
22

23 For a reaction process, the negative gradient of the potential energy $V(\xi)$ corresponds to the reaction
24 force $F(\xi)$. For a simple elementary step, the reaction force profile goes through a minimum in the
25 activation region (ξ_{\min}) and a maximum in the relaxation one (ξ_{\max}), which leads to a natural
26 partitioning of the reaction path into three regions: the R region ($\xi < \xi_{\min}$), the TS region ($\xi_{\min} < \xi <$
27 ξ_{\max}) and the P region ($\xi > \xi_{\max}$).⁶⁷⁻⁷²
28
29
30
31

32 To describe the DPT reaction from an orbital point of view, we used Natural Bond Orbital (NBO)
33 analysis⁷³⁻⁷⁵ which describes the stabilization of 3c-4e hydrogen-bonding as a consequence of
34 "donor-acceptor" interaction between a localized Lewis-type "donor" orbital (the lone-pairs n_B of the
35 Lewis base) and a non-Lewis-type "acceptor" orbital (the hydride anti-bonding $\sigma^*(\text{AH})$ of the Lewis
36 acid), for a A-H...B complex. The H-bond strength (or donor-acceptor delocalization energy) is
37 easily estimated by second order perturbation within NBO software.⁷⁶
38
39
40
41
42
43

44 In order to analyse the chemical bond evolution along the reaction path, we used the electron
45 localization function (ELF).⁷⁷ Indeed, the ELF topology⁷⁸ provides a partitioning of the molecular
46 space into chemically representative regions (basins of attractors)^{78,79} corresponding to the chemical
47 object in the framework of the Lewis valence theory⁸⁰⁻⁸⁵ and also in the Valence Shell Electron Pair
48 Repulsion (VSEPR) approach.⁸⁶⁻⁹⁰ During the last three decades, the ELF topology has been used to
49 characterize various types of chemical bonds^{80,87,91,92} and reaction mechanisms.^{93,94} Particularly, this
50 method was successfully applied to study different hydrogen-bonded complexes in the gas
51 phase.^{81,82,95-99} Within the ELF framework, the core-valence bifurcation (CVB) index is proposed to
52 distinguish strength of various kind of hydrogen bonds.¹⁰⁰ For a hydrogen bond (H-bond) complex
53
54
55
56
57
58
59
60

(usually noted as A-H...B, where A = proton donor, H = hydrogen, B = proton acceptor), this index is expressed as: $CVB = \eta_{cv} - \eta_{vv}$. η_{cv} corresponds to the ELF bifurcation value between ELF core domain and valence domain, while the η_{vv} stands for the ELF value at bifurcation point between $V(A,H)$ and $V(B)$. The last point is indeed a second order critical point (3,-1) linking the $V(A, H)$ proton-donor domain to the $V(B)$ proton-acceptor one.^{81,98}

The partition of the molecular space in terms of non-overlapping space-filling domains has been performed using the TopMod package.¹⁰¹ We used the Multiwfn package^{102,103} to evaluate both CVB and η_{vv} quantities. As shown recently by Silvi et al.,⁹⁸ the η_{vv} quantity enables us to estimate the variance of the $V(A-H)$ domain population. Consequently, we use now the η_{vv} quantity as a delocalization index.

The Bond-Evolution-Theory (BET)^{94-96,104-112} based on the ELF topology of reorganization of covalent bonds and lone pairs along the reaction path allows us to identify and describe most of the electronic events (such as bond breaking/forming and electronic density redistribution) which occur in the different regions delimited by the reaction force $F(\xi)$.

Results and discussions

I. The DPT reaction without external electric field

a. *On the nature of IRC at the TS plateau*

We re-investigate here the energy profile of the pyrazole–guanidine reaction (Figure 1, left), already discussed by Rauhut et al.⁵¹ It is worth noting that as the reactant and the product are identical, the profile is symmetric with respect to the transition state. The reaction force profile $F(\xi)$ is also displayed on Figure 1 (right). The extremum points of $F(\xi)$ located at $\xi = -1.48$ and $+1.48$ amu^{1/2}·Bohr delimit the transition region.^{67,71} Around the formal TS (where $\xi = 0$) extends the so-called “plateau” over 1.5 amu^{1/2}·Bohr the potential energy varies by less than 0.01 kcal/mol. **Indeed, the potential energy profile slightly varies with a small curvature at the plateau transition region (see Figure S1-b which shows the first and second derivatives of the potential energy over the plateau).** In order to make the double proton transfer visual, we also illustrated some structures at remarkable points on the energy profile (see Figure S1-a and Table S1) from which it appears that proton transfer of pyrazole begins quite before that of guanidine, in agreement with the asynchronous character of the concerted mechanism that the plateau suggests.

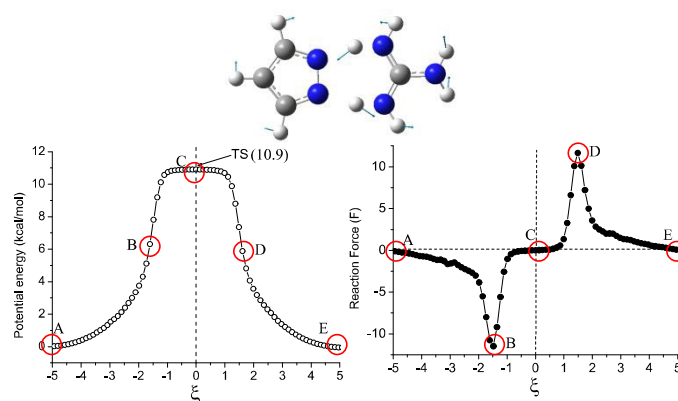


Figure 1. Energetic (left) and reaction force (right) profiles of the DPT reaction within the pyrazole-guanidine system.

The formal TS characterized by one small imaginary frequency ($61i \text{ cm}^{-1}$) is calculated to be 10.9 kcal/mol above the reactant. A visual checking of the atom displacement along the IRC path (Figure S1 and Table S1) shows that two normal modes are almost implicated along the reaction path: a low frequency asymmetric stretching mode of $\text{N}\cdots\text{N}$ heavy atoms observed almost on the plateau region, and a high frequency asymmetric stretching mode of two H atoms engaged in the DPT reaction.

To gain useful chemical insight on the reaction coordinate, we carried out two additional analyses on the IRC path: a principal component analysis (PCA) developed recently by Hare and coworker,¹¹³ and a Born-Oppenheimer molecular dynamics (BOMD) as implemented in the Gaussian package.⁵⁹

We used an open source Python package (*PathReducer*)¹¹³ to classify the principal components along the IRC path. As shown in Figure 2, only two principal components are necessary to capture 97% of the total variance in the double-proton transfer IRC structures (see Figure S3). The most significant principal component PC1 describes the asymmetric stretching mode of two H atoms engaged in the DPT reaction, while the second principal component represents the symmetric motion of two partners (see Figure S4 and Table S3). A close look to the reduced dimensional projection enables us to identify five distinct structures: A and E stand for the reactant and product structures, C for the formal TS structure, and B and D for two geometrical structures located at the minimum and maximum of the reaction force.

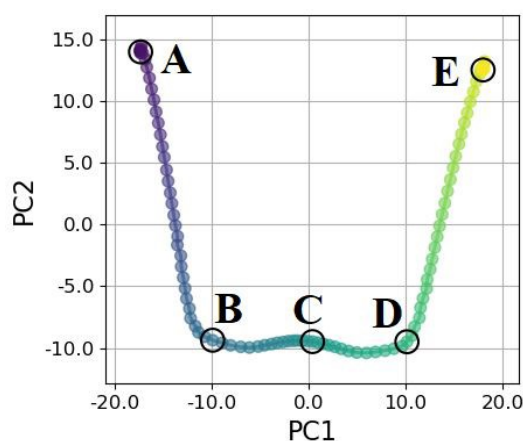
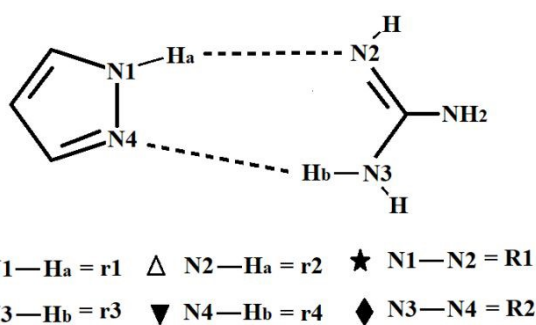


Figure 2. Projection of the double-proton transfer IRC structures in the two (reduced) dimensional space PC1 and PC2.

In order to gain a deeper insight over the B-C-D region, a new principal component analysis was performed, indicating clearly that only one PC is sufficient to describe all the structures in this region. This latter component, labeled as PC1 (TS-region), corresponds indeed to the asymmetric motion of N···N heavy atoms (see Figure S5 and Table S4).

In order to check the reliability of our static energetic profile (TS and IRC), the DPT reaction has been investigated also by dynamics (BOMD) quasiclassical trajectories (QCT) simulations. All QCTs were propagated up with a sufficient number of steps to obtain propagation times in the range of 51 to 53 fs.



Scheme 1: Atom and bond-length labeling within pyrazole-guanidine system.

Figure 3 shows the contour plots of the PES for the r_1 and r_3 coordinates (see Scheme 1 for the coordinate definition). Over twelve investigated reaction trajectories, starting from the formal TS structure, only eight reached the final structures: four in the reverse direction and four in the forward one. All contour plots are relative to the reactant energy ($0.0 \text{ kcal mol}^{-1}$). As the path reaction profile is perfectly symmetric, so we gathered all eight trajectories in the forward direction.

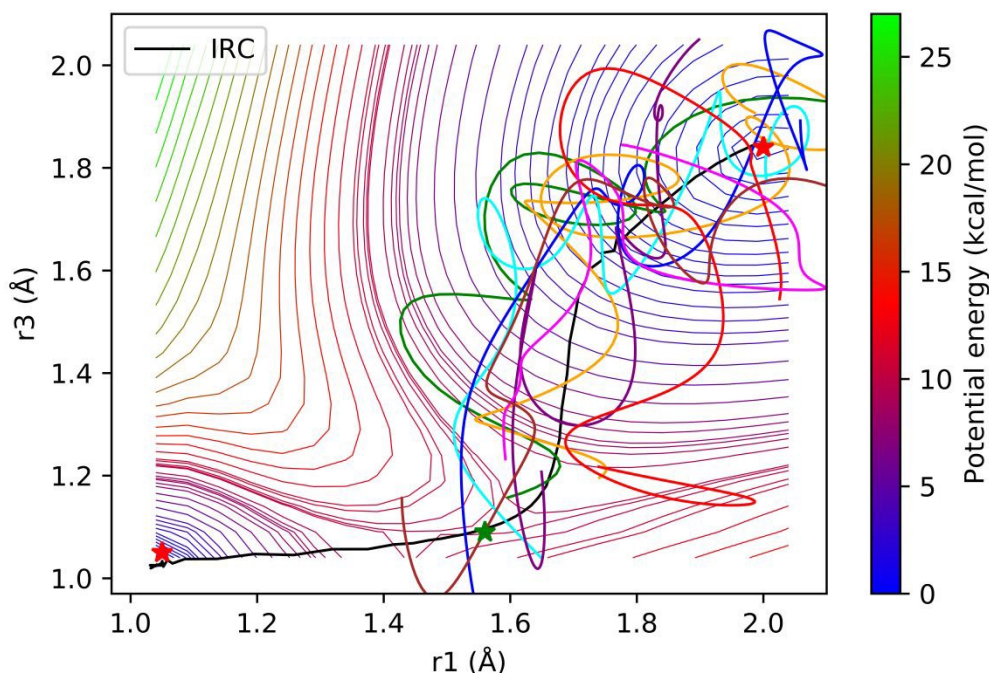
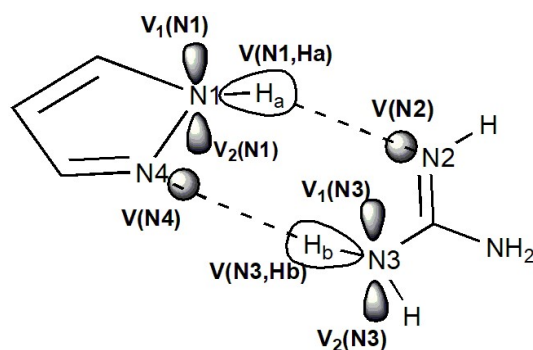


Figure 3. Relaxed potential energy curves (kcal/mol) as a function of the r_1 and r_3 coordinates (Å) for the pyrazole-guanidine DPT reaction. Relaxed scan were computed varying r_1 and r_3 coordinates in 0.05 Å steps. The black solid line corresponds to the IRC where TS (1.56, 1.10), Reactant (1.04, 1.02) and Product (2.0, 1.85) are indicated by asterisk symbol. Eight converged trajectories are also displayed.

A comparison between the static IRC and the reaction dynamics reveals the trajectories follow, on the average, the static minimum energy path (see Figure S6).

b. *Electronic aspects: the ELF valence basin evolution*

To make the discussion clearer, let us assign labels to all the valence basins which are directly involved in the double proton transfer reaction (see Scheme 2). We will use these labels throughout the rest of this paper during the ELF topological analysis.



Scheme 2. Labeling of the most relevant valence basins during DPT reaction.

The key ELF topological properties (electronic populations and number) of valence basins evolving within the DPT reaction over $\xi \in [-2.5, 0.0]$ segment are depicted in Figure 4. This interval of the

activation part of the reaction covers a piece of the reactant region ($\xi \in [-2.5, -1.5]$) and the half of the transition state region belonging to the activation part ($\xi \in [-1.5, 0.0]$). Due to the symmetry of the reaction, evolution of valence basins during the relaxation part of the reaction can easily be deduced from their evolution during the activation part, the role of H_a and H_b being reversed, as well as that of $N1$ and $N4$ and that of $N2$ and $N3$.

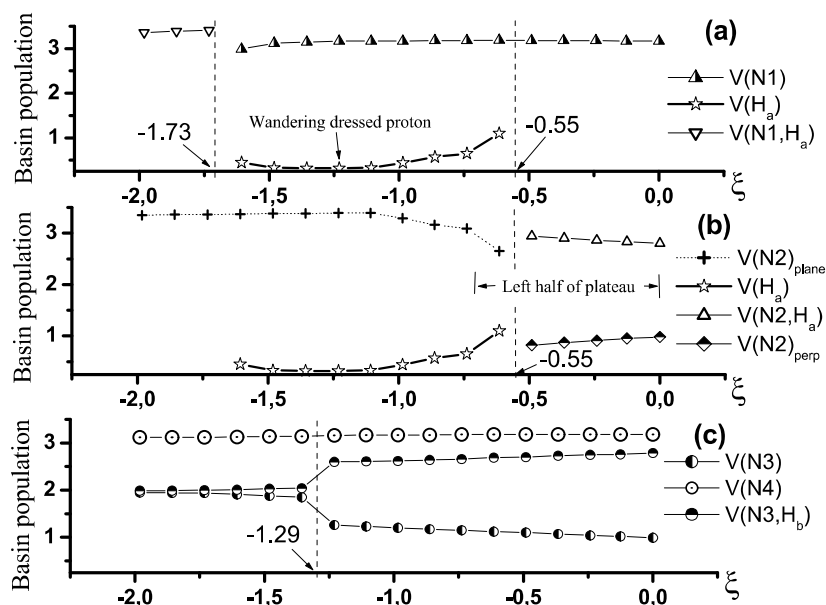


Figure 4. Elf basin populations and ELF basin shapes for some representative topological structures.

A close look at Figure 4 clearly reveals three distinct topological domains during which the first proton transfer (H_a) occurs.

- At the end of the first region, $\xi = -1.73 \text{ amu}^{1/2}$. Bohr (still in the reactant region as defined by the reaction force profile), the $V(N1, H_a)$ protonated disynaptic basin on pyrazole, splits into two distinct basins: a monosynaptic basin located on the $N1$ atom labeled as $V(N1)$ serving as lone-pair of nitrogen atom, and a detached hydrogen atom (labeled as H_a) which should be considered as a wandering “dressed proton”, because of its electronic population which amounts to around $0.5 e$ (Figure 4-a). Such a “dressed proton” transfer has already been identified and discussed in previous works in the case of single proton transfers.^{105,111}
- Along the second region ranging from -1.73 to $-0.55 \text{ amu}^{1/2}$. Bohr, the population of the wandering proton reaches its minimum value ($0.3 e$ at $\xi = -1.23 \text{ amu}^{1/2}$. Bohr).
- The topological evolution of the “wandering proton” presents a fine structure within the third region precisely at $\xi = -0.5 \text{ amu}^{1/2}$. Bohr, slightly after the plateau starting point. The population of $V(H_a)$ increases along $\xi \in [-1.23, -0.5]$ interval and merges with $V(N2)_{\text{plane}}$

basin in forming a new disynaptic basin, $V(N2,H_a)$. As shown in Figure 4-b the population of $V(N2,H_a)$ amounts to around 3 e, over $\xi \in [-0.5, 0]$. Simultaneously, the population of the monosynaptic basin located on the N2 atom of guanidine, $V(N2)$, decreases from 3 e to 1 e. In other words, the protons are actually transferred at the edges of the plateau while at the center of the plateau the reaction is dominated by a local reorganization of the lone-pairs of the protonated N atoms of guanidine (see Figure S2-a, S2-b and Table S2 for detailed information).

Concomitantly, as displayed in Figure 4-c the population of the monosynaptic basin (lone-pair) $V(N4)$ hardly changes, over the whole of $\xi \in [-2.5, 0.0]$ segment. However, the population of the two valence basins $V(N3)$ and $V(N3,H_b)$ show a small change of the order of 0.5 e. As a result, the population of the monosynaptic basin (lone-pair) $V(N3)$ decreases from 2 e to 1.2 e, while that of the disynaptic protonated basin $V(N3,H_b)$ increases from 2 e to 2.8 e. This is the topological indication of upcoming changes along the reaction path where $\xi > 0$. Accordingly, at the formal TS point ($\xi = 0$) the pyrazole–guanidine system corresponds actually to a couple of ionic compounds: deprotonated pyrazole (pyrazolate) in interaction with protonated guanidine (guanidinium).

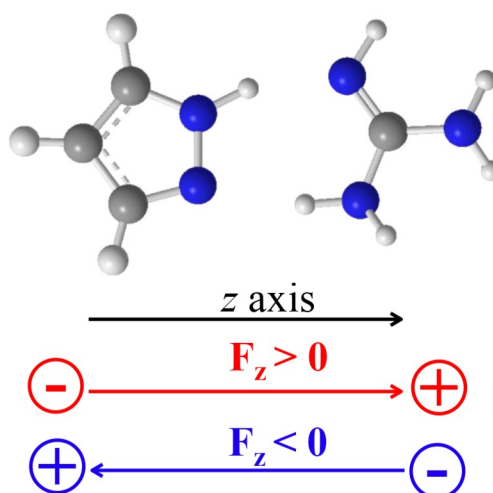
II. OEEF effects on the DPT reaction

In this section, we will analyze the effect of an OEEF on the principal features of the pyrazole–guanidine DPT reaction. We will first present our investigations for negative OEEFs ($F_z < 0$), then we will analyze the effects of positive OEEFs ($F_z > 0$). In Table 1 are gathered the modulus of electric field in various units.

Gaussian	au	MV.cm ⁻¹	V.m ⁻¹ ($\times 10^9$)
20	0.002	10.28	1.03
40	0.004	20.56	2.06
60	0.006	30.84	3.08
80	0.008	41.12	4.11
100	0.010	51.40	5.14

Table 1. The modulus of the applied electric fields in different units.

In Scheme 3 is illustrated the convention for the OEEF orientation and polarity used in this work. F_z represents the external electric field applied in the Z direction.



Scheme 3. The polarity convention for the OEEF in Gaussian.

1) From concerted asynchronous to stepwise DPT reaction: F_z in negative Z-direction

Equilibrium geometry and IRC analysis along the reaction pathway have been studied for the pyrazole–guanidine complex using five negative values for F_z : -20, -40, -60, -80, and -100 ($\times 10^{-4}$ au).

a. *Energetic and geometrical aspects*

As shown in Figure 5, application of a negative field radically transforms the reaction mechanism. We observe the appearance of a reaction intermediate (RI) in the center of the plateau resulting from a single proton transfer (H_a) and whose stability increases as the electric field intensity increases. It is accompanied by the appearance of a first transition state between reactant and reaction intermediate on the left side of the initial plateau ($F_z = 0$) and a second one between the reaction intermediate and the product, on the right side. Due to the symmetry of the system, we only show a half part of the energy profiles (see Figure S7). The barrier height decreases with increasing electric field strength: it varies from 10.2 to 1.5 kcal.mol⁻¹ when F_z goes from 0 to -100×10^{-4} au. For this extreme electric field strength, the RI is by 2.9 kcal.mol⁻¹ more stable than the pyrazole–guanidine complex. In other words, the concerted mechanism ($F_z = 0$) definitely becomes a stepwise mechanism when $F_z < -80 \times 10^{-4}$ au. In particular, RI potentially becomes the only product of the pyrazole + guanidine reaction observable in an experiment at $F_z = -100 \times 10^{-4}$ au.

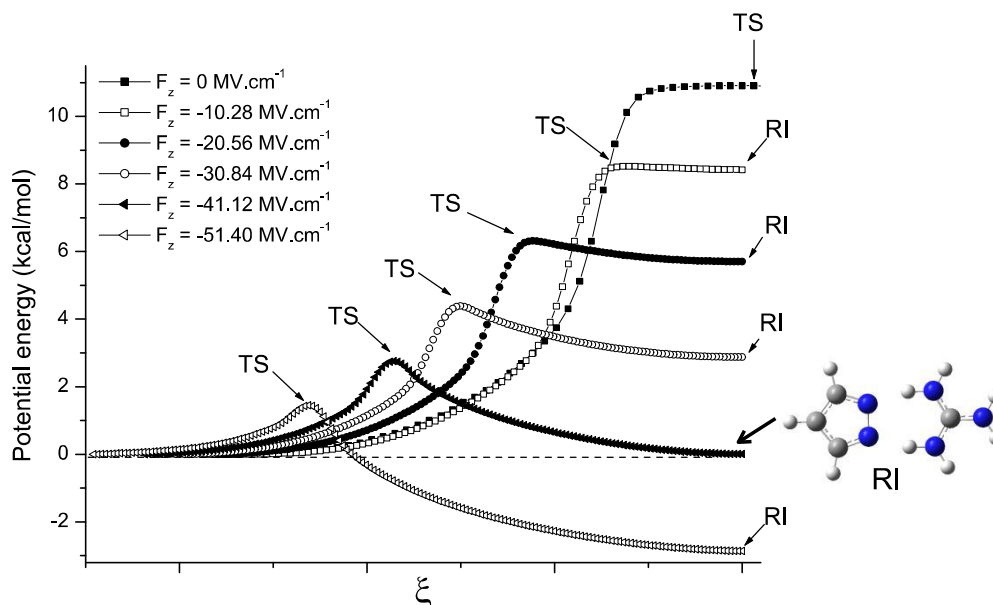


Figure 5. IRC profiles for various negative values of F_z .

A summary of selected bond lengths is shown in Table 2 (please, see Scheme 1 for bond-length labeling). For the reactant, it is easy to note that the two proton donor bond lengths (r_1 on pyrazole and r_3 on guanidine) vary in the opposite direction of each other when the electric field changes from -20×10^{-4} to -100×10^{-4} au: r_1 lengthens by about 0.03 \AA , while r_3 shortens by about 0.01 \AA . Such a geometrical change under the effect of electric field has been discussed in the case of hydrogen-bonded acid-base complexes.^{2,14,20,21,44,114} These changes are also concomitant with a notable increase of R_2 ($\sim 0.5 \text{ \AA}$), and a smaller decrease of R_1 of about 0.1 \AA . When the compression of one hydrogen bond leads to the elongation of the second one, two coupled hydrogen bonds are said to be anti-cooperative.^{115,116} As the F_z intensity increases, the RI stabilizes more and more, and the TS which looks like the RI for $F_z = -20 \times 10^{-4}$ au ended up looking like the reactant, in agreement with Hammond's postulate. Finally, it should be noted that in the RI, the distance r_2 was found to be very close to the bond length r_3 for the five negative values of F_z , which is characteristic of a protonated guanidine.

$F_z(\times 10^4)$ au	$r_1(\text{\AA})$	$r_2(\text{\AA})$	$r_3(\text{\AA})$	$r_4(\text{\AA})$	$R_1(\text{\AA})$	$R_2(\text{\AA})$
Reactant structure						
0	1.033	1.834	1.020	2.005	2.827	3.002
-20	1.039	1.793	1.017	2.061	2.799	3.054
-40	1.045	1.753	1.015	2.114	2.773	3.101
-60	1.054	1.712	1.013	2.157	2.746	3.139
-80	1.063	1.673	1.011	2.263	2.724	3.238
-100	1.072	1.642	1.008	2.524	2.710	3.481

Transition structure							
0	1.562	1.097	1.097	1.562	2.634	2.634	
-20	1.451	1.146	1.054	1.720	2.580	2.743	
-40	1.381	1.191	1.038	1.813	2.557	2.815	
-60	1.334	1.227	1.028	1.898	2.549	2.886	
-80	1.291	1.266	1.021	1.982	2.548	2.960	
-100	1.252	1.308	1.016	2.085	2.553	3.054	
Reaction intermediate							
-20	1.598	1.084	1.078	1.619	2.659	2.673	
-40	1.650	1.070	1.068	1.659	2.696	2.703	
-60	1.651	1.070	1.068	1.658	2.697	2.702	
-80	1.743	1.050	1.050	1.743	2.772	2.771	
-100	1.790	1.043	1.043	1.791	2.812	2.813	

Table 2. Key bond lengths of pyrazole-guanidine system subjected to $F_z < 0$ at three stationary points. Please, see Scheme 1 for bond-length labeling.

b. *BET analysis*

From the ELF topological point of view, the geometrical changes are related to the topological changes of valence basins. For the reactant structure, these changes mainly concern the three valence basins on the N1 atom: V1 (N1), V2 (N1) and V (N1, Ha). As long as the F_z strength lies between 0 and -40×10^{-4} au, the two basins $V_1(N1)$ and $V_2(N1)$ are equally populated (~ 0.5 e) while the population of V(N1, Ha) is 2.3 e. For $F_z = -40 \times 10^{-4}$ au, a topological change occurs: the two valence basins $V_1(N1)$ and $V_2(N1)$ disappear in favor of the V(N1, Ha) whose population increases by 1 e ($V(N1, Ha) = 3.3$ e). The same feature holds for the $F_z = -60 \times 10^{-4}$, -80×10^{-4} , and -100×10^{-4} au. For these different values of F_z , the valence basins centered on atom N3 remain unchanged.

In order to describe the bond topological evolution along the reaction path, we will limit ourselves to the case $F_z = -80 \times 10^{-4}$ au. This description is obviously transposable to other negative electric fields. In Figure 6 are displayed the most relevant topological changes on the proton donor bond of pyrazole from $\xi = -2.5$ to 3.5 $\text{amu}^{1/2} \cdot \text{Bohr}$, which covers the transition from reactant to reaction intermediate passing through the transition state ($\xi = 0$). As shown clearly in Figure 6, three regions are to be distinguished on the $\xi \in [-2.5$ to 3.5 $\text{amu}^{1/2} \cdot \text{Bohr}]$ interval, corresponding to three topological domains of the same structural stability. The three regions are separated by two critical distances $r_1 = r(N1-Ha) = 1.097$ Å (separation between first and second regions) and $r_2 = r(N1-Ha) = 1.486$ Å (separation between second and third regions).

In the first region extending from $\xi = -2.5$ to -0.5 $\text{amu}^{1/2}\cdot\text{Bohr}$, $V(\text{N1},\text{H}_a) \cong 3.3$ e is the unique valence basin on the nitrogen atom of the pyrazole proton donor bond. It is worth noting that such a protonated valence basin with a population exceeding 2.5 e is topologically unstable which might evolve towards another structurally stable domain.⁹⁷ At $\xi = -0.5$ $\text{amu}^{1/2}\cdot\text{Bohr}$, the $V(\text{N1},\text{H}_a)$ protonated valence basin splits into two new valence basins: a basin centered on nitrogen atom standing to the lone-pair ($V(\text{N1}) \cong 1.5$ e), and a wandering “dressed proton” of a population close to 0.5 e (see Figure 6-a).

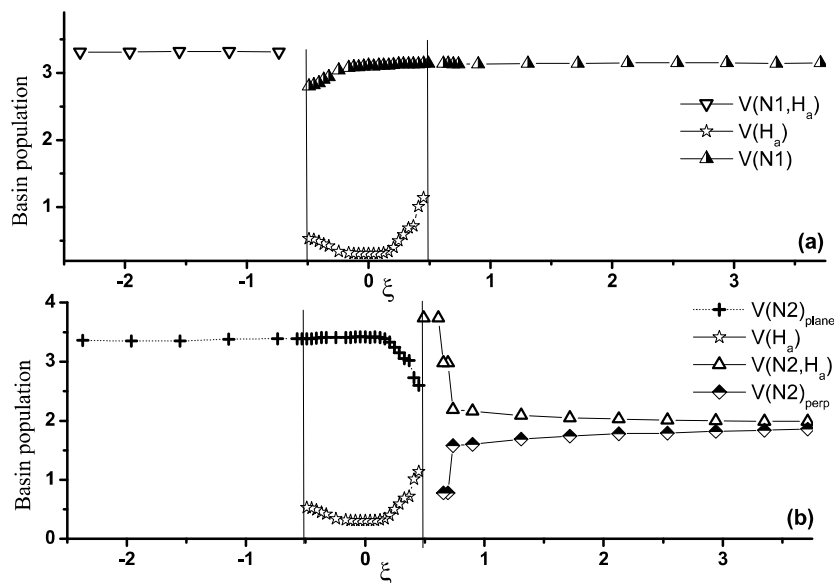


Figure 6. ELF population evolution on the reaction pathway from reactant to reaction intermediate for $F_z = -80 \times 10^{-4}$ au.

At the end of the second region, close to $\xi = 0.5$ $\text{amu}^{1/2}\cdot\text{Bohr}$, not only the $V(\text{N1})$ reaches its equilibrium value, 3.3 e, but also the wandering proton merges with $V(\text{N2})_{\text{plane}}$ to form two new valence basins: one for the freshly formed chemical bond labeled as $V(\text{N2}, \text{H}_a)$, and the other for the non-bonding electron located on nitrogen atom perpendicular to the plane of the complex, $V(\text{N2})_{\text{perp}}$. Finally, during the third region extending from $\xi = 0.5$ to 3.5 $\text{amu}^{1/2}\cdot\text{Bohr}$, the population of these basins converges rapidly towards 2 e (see Figure 6-b). The compound stabilized at the end of this process is actually made up of two interacting ions: pyrazolate and guanidinium.

2) From concerted asynchronous to synchronous DPT reaction: F_z in positive Z-direction

Equilibrium geometry and IRC analysis along the reaction pathway have also been studied for the pyrazole–guanidine complex using four positive values for F_z : 20, 40, 60, and 80 ($\times 10^{-4}$ au).

a. Energetic and geometrical aspects

As shown in Figure 7, all the energy profiles remain symmetric with respect to the transition state (where $\xi = 0$) when applying a positive electric field in agreement with the fact that R and P remain identical. It is clearly noticeable that the barrier height increases from 10.9 to 15.2 kcal.mol⁻¹ when F_z varies from 0 to 40×10^{-4} au (see Figure 7-a). This rise of the barrier height is accompanied by a decrease of the plateau width from 1.50 toward 0 amu^{1/2}.Bohr, where the "plateau transition state" becomes a standard transition state with a well-defined transition structure. Accordingly, the near extinction of the "plateau transition region" for $F_z \approx 40 \times 10^{-4}$ au transforms an asynchronous pyrazole–guanidine DPT reaction to a near synchronous one. For the higher intensities of OEEF, the activation barrier decreases from 15.2 to 12.1 kcal.mol⁻¹, and the plateau comes back until $F_z = 80 \times 10^{-4}$ au for which the plateau width is 1.4 amu^{1/2}.Bohr. Therefore, the DPT reaction switches back to an asynchronous regime.

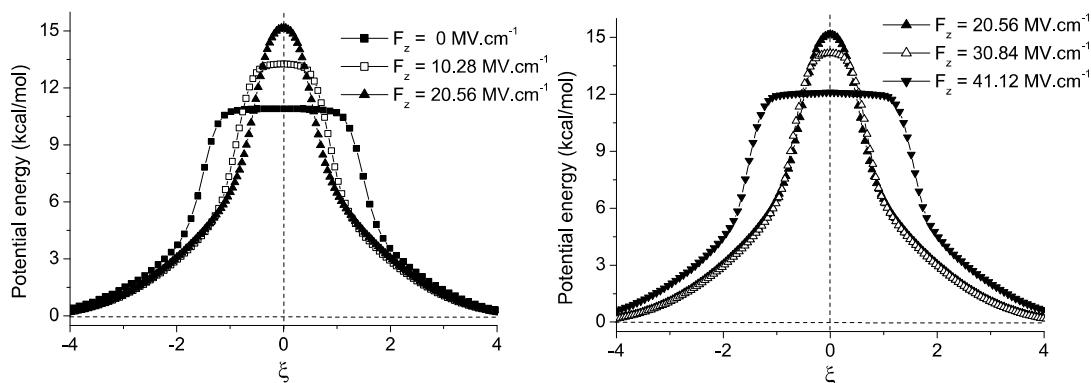


Figure 7. IRC profiles for various positive values of F_z .

At this point, we will study the geometric changes in the key bond lengths of the pyrazole-guanidine system subjected to $F_z > 0$. In Table 3 are reported the values of six bond-distances as function of the field strength F_z for two particular geometries along the reaction path (reactant and transition state), using the labels defined in Scheme 1.

$F_z(\times 10^{-4})$ au	r1(Å)	r2(Å)	r3(Å)	r4(Å)	R1(Å)	R2(Å)
	$(H_a \text{ transfer})$		$(H_b \text{ transfer})$			
	Reactant structure					
0	1.033	1.834	1.020	2.004	2.827	3.002
20	1.028	1.885	1.022	1.960	2.861	2.964
40	1.023	1.928	1.025	1.928	2.891	2.935
60	1.020	1.982	1.029	1.884	2.926	2.897
80	1.016	2.047	1.033	1.846	2.971	2.865
	Transition structure					

0	1.562	1.097	1.097	1.562	2.634	2.634
20	1.507	1.118	1.120	1.502	2.600	2.600
40	1.423	1.163	1.164	1.422	2.560	2.560
60	1.124	1.504	1.502	1.124	2.587	2.587
80	1.097	1.572	1.571	1.098	2.624	2.624

Table 3. Key bond lengths of the pyrazole-guanidine system subjected to $F_z > 0$ at two stationary points.

First of all, it is worth noting that at $F_z = 0$, in the reactant structure, the r2 hydrogen bond distance (1.83 Å) is significantly shorter than the r4 one (2.00 Å). It is consistent with a $N2 \cdots H_a$ hydrogen bond stronger than $N4 \cdots H_b$ and therefore an H_a proton transferred in advance of H_b as mentioned above.

In the reactant structure, the pyrazole N–H bond length (r1) shrinks when F_z increases, while we observe an elongation of the guanidine N–H bond length (r3) engaged in the H-bond interaction. As a consequence, the N-H bond length (r3) at $F_z = 80 \times 10^{-4}$ au becomes equal to that of r1 at $F_z = 0$ and the other way around. r2 and r4 hydrogen bond distances also vary in opposite directions as function of F_z : r2 increases while r4 decreases as F_z increases, in such a way that the r4 hydrogen bond distance at $F_z = 80 \times 10^{-4}$ au becomes almost equal to that of r2 at $F_z = 0$ and r2 at $F_z = 80 \times 10^{-4}$ au equal to r4 at $F_z = 0$. This is a first element suggesting that at $F_z = 80 \times 10^{-4}$ au proton H_b is transferred in advance on proton H_a . Interestingly, at $F_z = 40 \times 10^{-4}$ au, where the double proton transfers take place in a synchronous way, $r1 \cong r3$ and $r2 = r4$, indicating that both hydrogen bonds are of similar strength. For N–N distances, R1 increases while R2 decreases as F_z increases.

For the transition structure, $r1 \cong r4$ and $r2 \cong r3$, *i.e.* both protons are equidistant of the two N atoms of the same molecule. For $F_z \leq 40 \times 10^{-4}$ au, both protons are closer to guanidine than to pyrazole, meaning that the transition structure is late for H_a transfer but early for H_b on. On the contrary, for $F_z > 40 \times 10^{-4}$ au, both protons are closer to pyrazole than guanidine, in agreement with a transition structure late for H_b transfer but early for H_a one. Concomitantly, $R1 \cong R2$ for all positive values of F_z . Particularly, for the field strength $F_z = 40 \times 10^{-4}$ au (synchronous mechanism), we should underline that the N-N distance ($R1=R2$) reaches its minimum value ($R1=R2=2.560$ Å).

b. *BET analysis*

Here, we limit ourselves to a concise study of major changes over an IRC segment which extends from $\xi \approx -2.5$ amu^{1/2}·Bohr to $\xi = 0$ (transition state), *i.e.* rising flank. We remember that the same topological changes occur over the falling flank of the energetic profile.

- $F_z = 20 \times 10^{-4}$ au

Inspection of the evolution of the ELF topology along the reaction pathway reveals that the

protonated disynaptic basin, $V(N1,H_a)$, splits close to $\xi \approx -1 \text{ amu}^{1/2}\cdot\text{Bohr}$ into two new basins: $V(N1)$ and $V(H_a)$ standing for the lone-pair and a wandering proton, respectively (see Figure 8-a). $V(H_a)$ basin carrying a very small population merges with $V(N2)$ when $\xi = 0$ (formal TS) to form a new protonated disynaptic basin, $V(N2,H_a)$, accomodating around of 3 electrons (Figure 8-b). During the $\xi \in [-2.5, 0 \text{ amu}^{1/2}\cdot\text{Bohr}]$ interval, the lone-pair basin on the N4 atom remains unchanged, while the $V(N3)$ and $V(N3,H_b)$ populations changes slightly at $\xi \approx -0.6 \text{ amu}^{1/2}\cdot\text{Bohr}$ (Figure 8-c).

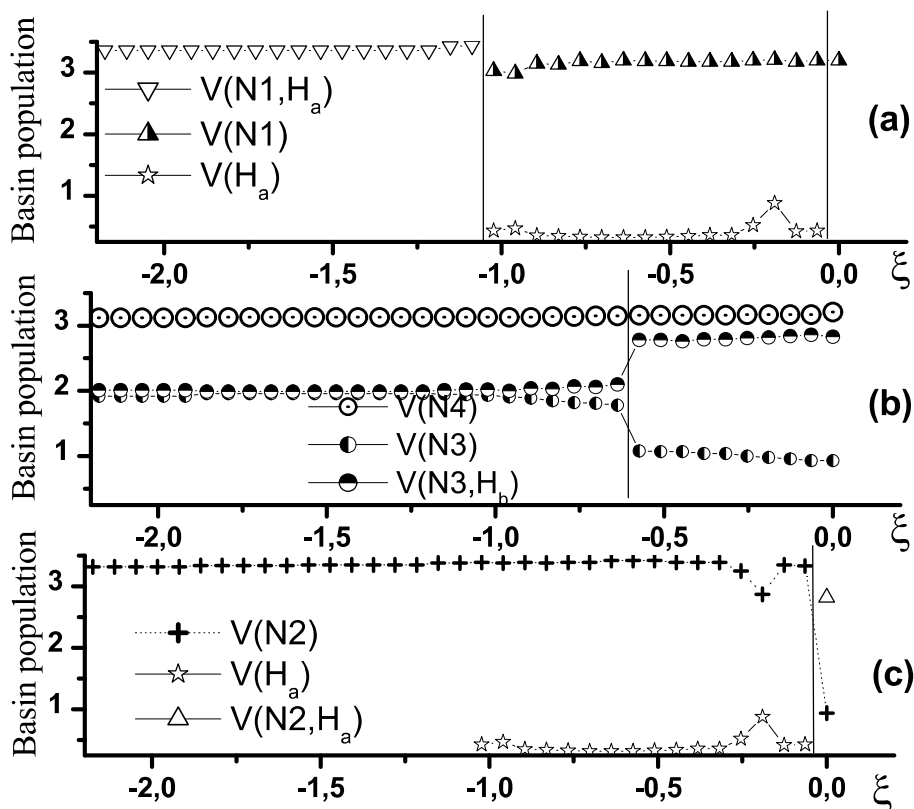


Figure 8. ELF population evolution on the rising flank of the energetic profile for $F_z=20\times 10^{-4} \text{ au}$.

At $\xi = 0$ (formal TS), we have a deprotonated pyrazole–protonated guanidine couple, similar to case $F_z = 0$. Immediately one step after TS, $\xi = 0.06 \text{ amu}^{1/2}\cdot\text{Bohr}$, the $V(N3,H_b)$ bond breaks and the second proton transfer process begins.

- $F_z = 40\times 10^{-4} \text{ au}$

In this case, although the electronic reorganization during the DPT reaction is very similar to that discussed in the previous paragraph, we must however point out some notable differences. First, detachment of the two protons occurs before TS: at $\xi = -0.69 \text{ amu}^{1/2}\cdot\text{Bohr}$ for the first proton (H_a) from the pyrazole side, and at $\xi = -0.22 \text{ amu}^{1/2}\cdot\text{Bohr}$ for the second proton (H_b) from the guanidine

side. Second, the formation of two new bonds occurs only after TS. In other words, at TS the system consists of three partners: two wandering “dressed protons” in sandwich between a deprotonated pyrazole and a deprotonated guanidine (see Figure 9).

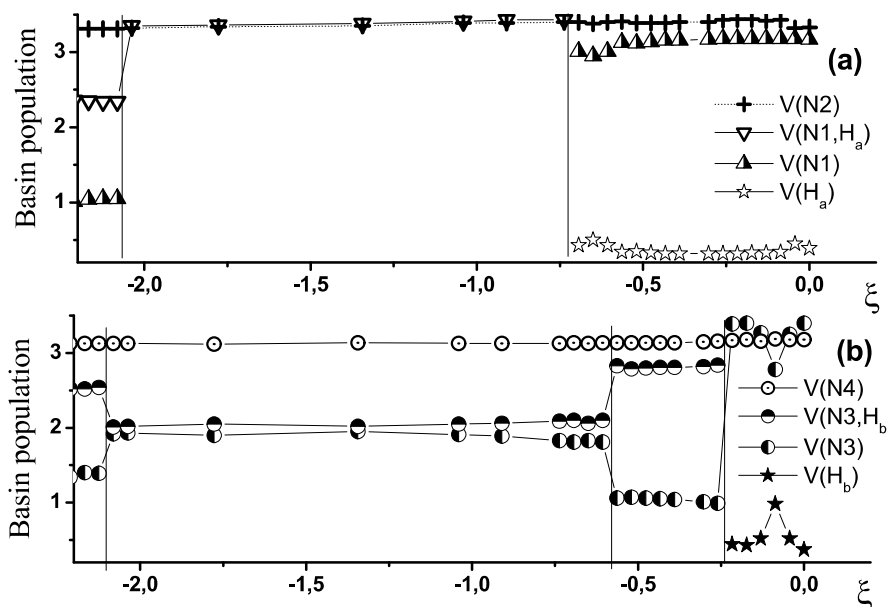


Figure 9. ELF population evolution on the rising flank of the energetic profile for $F_z=40 \times 10^{-4}$ au.

- $F_z = 60 \times 10^{-4}$ au

As illustrated in Figure 10, for this strength of the electric field, it is the guanidine N3- H_b proton that breaks off first at $\xi = -0.80$ amu^{1/2}·Bohr, while the proton detachment from the pyrazole side occurs only one step before the TS ($\xi = -0.05$ amu^{1/2}·Bohr). This is in agreement with the evolution of N---H distances discussed above. This feature can be explained by the fact that positive electric fields make the detachment of the proton from pyrazole more difficult (the corresponding hydrogen bond in the reactive complex is weakened) and the detachment of the proton from guanidine easier (the corresponding hydrogen bond in the reactive complex is strengthened).

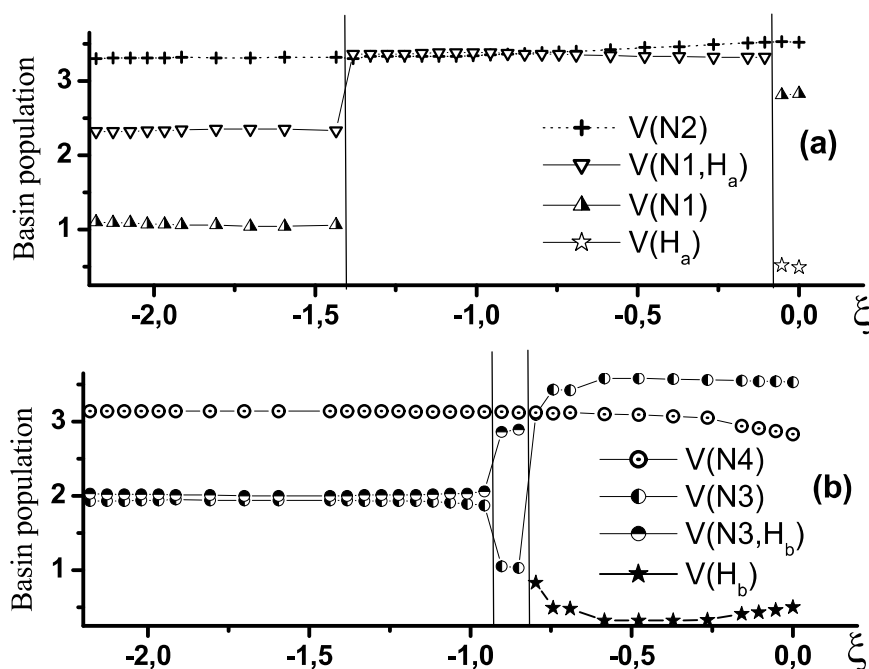


Figure 10. ELF population evolution on the rising flank of the energetic profile for $F_z=60 \times 10^{-4}$ au.

- $F_z = 80 \times 10^{-4}$ au

With this electric field, the N3-H_b bond breaks to an even smaller value of IRC ($\xi = -1.66$ amu^{1/2}·Bohr) than with $F_z = 60 \times 10^{-4}$ au (see Figure 11). From an energetic point of view, the energy required to break the N3-H_b bond is smaller with $F_z = 80 \times 10^{-4}$ au than with $F_z = 60 \times 10^{-4}$ au (6.6 kcal.mol⁻¹ at $\xi = -1.66$ amu^{1/2}·Bohr vs. 8.8 kcal.mol⁻¹ at $\xi = -0.80$ amu^{1/2}·Bohr).

At formal TS, the system consists on a protonated pyrazole and a deprotonated guanidine.

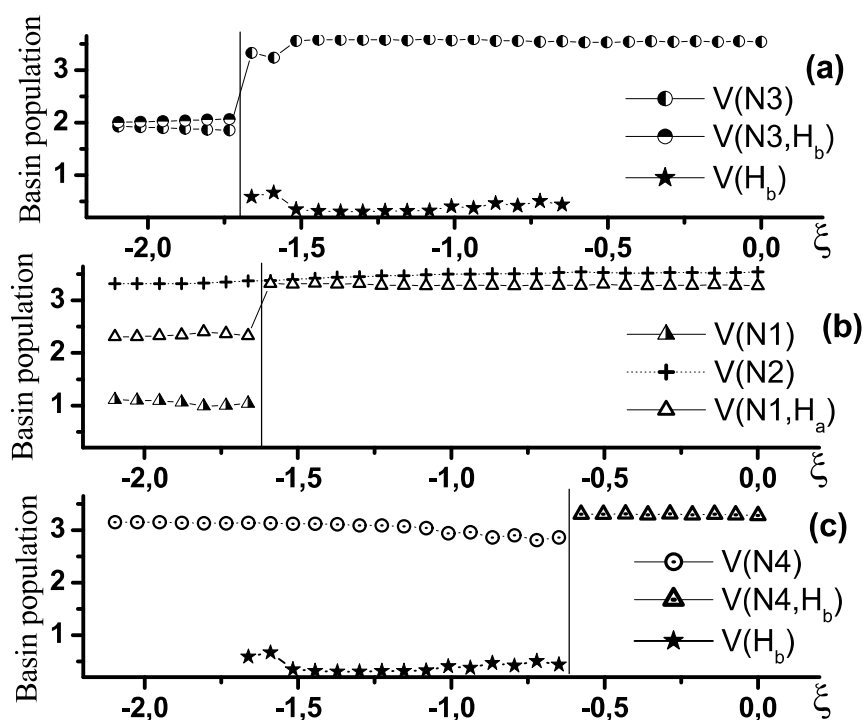


Figure 11. ELF population evolution on the rising flank of the energetic profile for $F_z=80\times 10^{-4}$ au.

Consequently, the positive electric field transforms a “plateau asynchronous DPT reaction” to a “synchronous DPT reaction” for $F_z \approx 40\times 10^{-4}$ au, and then to a new “plateau asynchronous DPT reaction” for $F_z > 40\times 10^{-4}$ au. The pyrazole–guanidine system should be considered as deprotonated pyrazole in interaction with protonated guanidine at the TS when $0 < F_z < 40\times 10^{-4}$ au, and as protonated pyrazole in interaction with deprotonated guanidine at the TS when $40\times 10^{-4} < F_z < 80\times 10^{-4}$ au. As expected,² this characteristic feature can be correlated with the polarity of the electric dipole at the TS structures in function of the positive electric field intensity (see Figure 12). The Z-component of the dipole moment changes sign for a value of F_z between 40×10^{-4} au and 50×10^{-4} au. Indeed, the DPT reaction mechanism changes for a value of F_z within this interval in passing from an asynchronous to synchronous mechanism, and then again from a synchronous to asynchronous regime.

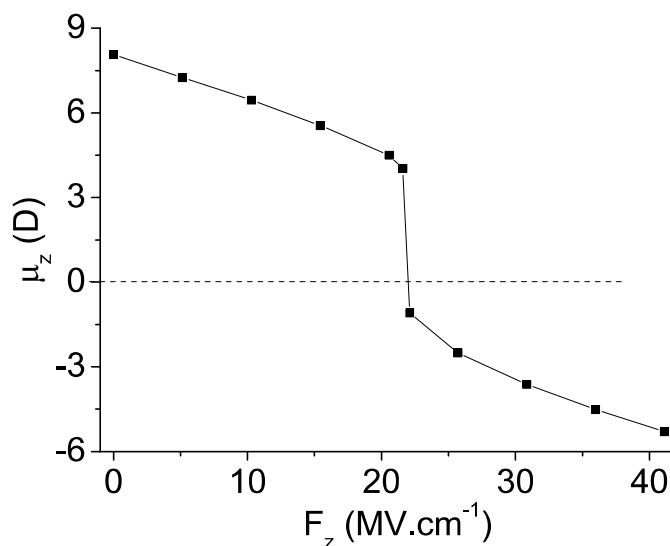


Figure 12. Variation of the Z-component of the total electric dipole (in D) as a function of electric field strength at the TS structure.

3) ELF hydrogen bond interaction bifurcation (η_{vv}): a topological predictive descriptor

Figure 13 depicts the ELF isolines of the pyrazole–guanidine complex in the entrance channel, in the absence of electric field, for two ELF values (a) ELF = 0.12 and (b) ELF = 0.20, which correspond to two critical points of index 1 marked in red circles.⁹⁸

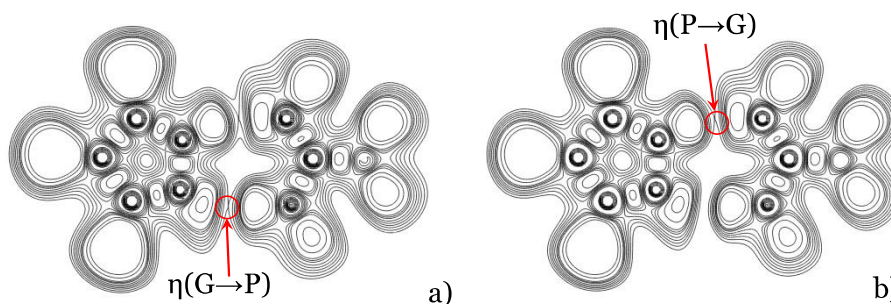


Figure 13. 2D ELF isolines of the pyrazole-guanidine complex in the entrance channel in the absence of electric field. (a) ELF = 0.12, (b) ELF = 0.20. The ELF hydrogen bond interaction bifurcations are marked in red circles.

The critical point of the hydrogen bond appears at a smaller ELF value when guanidine is the proton donor than that of the hydrogen bond when pyrazole is the proton donor. This clearly means that in the absence of electric field, pyrazole is a better proton donor than guanidine in the studied complex. This simple consideration is in line with the fact that in the absence of electric field, the first proton transfer occurs from pyrazole to guanidine along the reaction path.

According to the NBO analysis, donor–acceptor interactions are quantified in terms of the perturbative energy lowering which could be used as a measure of the hydrogen-bond strength.^{74,75} For the double hydrogen bonded pyrazole–guanidine complex (both reactant and product), two

moderate donor–acceptor interaction energies have been calculated in the absence of electric field: $E_2(\text{pyrazole nitrogen lone-pair} \rightarrow \text{antibonding N-H on the guanidine}) = 13.4$, and $E_2(\text{guanidine nitrogen lone-pair} \rightarrow \text{antibonding N-H on the pyrazole}) = 28.7 \text{ kcal.mol}^{-1}$ (see Figure S8).

The ELF bifurcation (η_{vv}) and NBO interaction energies (E_2) for the two hydrogen bonds of the pyrazole–guanidine reactant, as well as the barrier height of reactant–product reaction under the influence of an OEEF are gathered in Table 4. $\eta_{(\text{P} \rightarrow \text{G})}$ stands for the ELF bifurcation when pyrazole is a proton donor, and $\eta_{(\text{G} \rightarrow \text{P})}$ represents the ELF bifurcation when guanidine is a proton donor. The difference between the two bifurcation values is labeled as $\delta\eta = \eta_{(\text{P} \rightarrow \text{G})} - \eta_{(\text{G} \rightarrow \text{P})}$. Similarly, the difference between two NBO interaction energies is labeled as $\delta E_2 = E_{2(\text{P} \rightarrow \text{G})} - E_{2(\text{G} \rightarrow \text{P})}$.

F_z ($\times 10^4 \text{ au}$)	ELF: η_{vv}		NBO: E_2 (kcal.mol^{-1})		ELF: $\delta\eta$	NBO: δE_2 (kcal.mol^{-1})	Barrier height (kcal.mol^{-1})
	$\eta_{(\text{P} \rightarrow \text{G})}$	$\eta_{(\text{G} \rightarrow \text{P})}$	$E_{2(\text{P} \rightarrow \text{G})}$	$E_{2(\text{G} \rightarrow \text{P})}$			
100	0.092	0.203	9.50	27.63	-0.111	-18.13	10.4
80	0.111	0.190	12.90	24.78	-0.079	-11.88	12.1
70	0.122	0.181	14.68	23.38	-0.059	-8.70	13.1
60	0.134	0.169	16.44	20.90	-0.035	-4.46	14.1
50	0.142	0.161	18.32	19.82	-0.019	-1.50	15
40	0.152	0.151	20.08	18.43	0.001	1.65	15.1
30	0.165	0.143	21.95	17.17	0.022	4.78	14.2
20	0.175	0.135	23.78	15.83	0.040	7.95	13.2
10	0.185	0.131	26.43	14.67	0.054	11.76	12
0	0.200	0.123	28.73	13.37	0.077	15.36	10.9
-20	0.222	0.107	33.96	10.97	0.115	22.99	8.5
-30	0.235	0.098	36.48	9.87	0.137	26.61	7.4
-40	0.251	0.09	39.32	8.93	0.161	30.39	6.3
-50	0.265	0.086	42.62	8.27	0.179	34.35	5.3
-60	0.278	0.077	46.28	8.14	0.201	38.14	4.4
-80	0.310	0.061	54.00	6.22	0.249	47.78	2.8
-100	0.350	0.045	64.01	4.42	0.305	59.59	1.5

Table 4. ELF and NBO values at the hydrogen bond between pyrazole and guanidine system subjected to an electric field. $\delta\eta = \eta_{(\text{G} \rightarrow \text{P})} - \eta_{(\text{P} \rightarrow \text{G})}$ and $\delta E_2 = E_{2(\text{P} \rightarrow \text{G})} - E_{2(\text{G} \rightarrow \text{P})}$. Barrier height (in kcal.mol^{-1}) is the required energy in going from reactant to product.

As expected, the two interacting partners behave in an opposite way to each other under the electric field.

- When positive electric field increases, $\eta_{(\text{P} \rightarrow \text{G})}$ decreases while $\eta_{(\text{G} \rightarrow \text{P})}$ increases. Consequently, the proton donor capacity of pyrazole decreases while that of guanidine increases. For

$F_z=40\times 10^{-4}$ au, we get $\eta_{(P\rightarrow G)} \cong \eta_{(G\rightarrow P)}$ indicating a similar deprotonation capacity of both partners, which leads to a synchronous mechanism.

- When the negative electric field intensity increases, $\eta_{(P\rightarrow G)}$ increases while $\eta_{(G\rightarrow P)}$ decreases. Consequently, the deprotonation ability of pyrazole which was already superior to that of guanidine increases again ($\eta_{(P\rightarrow G)}$ increases) while that of guanidine declines, leading to the formation of a zwitterionic reaction intermediate in which guanidine is protonated (guanidinium) and pyrazole deprotonated (pyrazolate).

Figure 14 illustrates the variation of $\delta\eta$ as a function of the electric field intensity. The difference between the two ELF bifurcations corresponding to both hydrogen bonds, $\delta\eta$, linearly decreases when F_z goes up from -100×10^{-4} to 80×10^{-4} au, with a very good correlation coefficient ($R^2 = 0.997$)

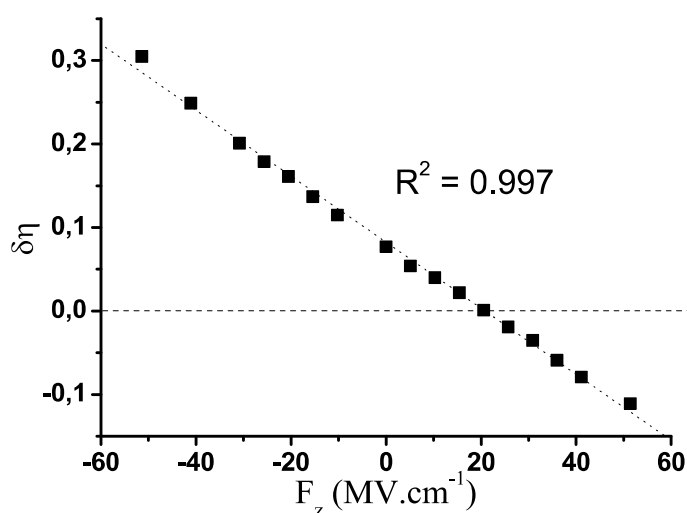


Figure 14. Variation of $\delta\eta$ in function of F_z .

As shown in Figure 15, $\delta\eta$ varies linearly also with δE_2 ($R^2=0.999$).

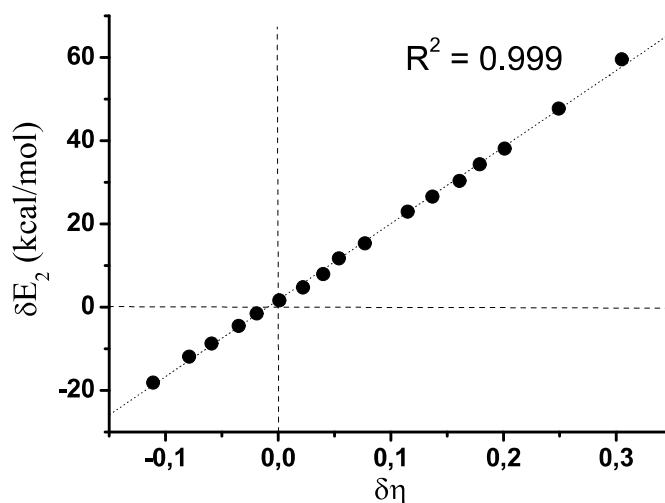
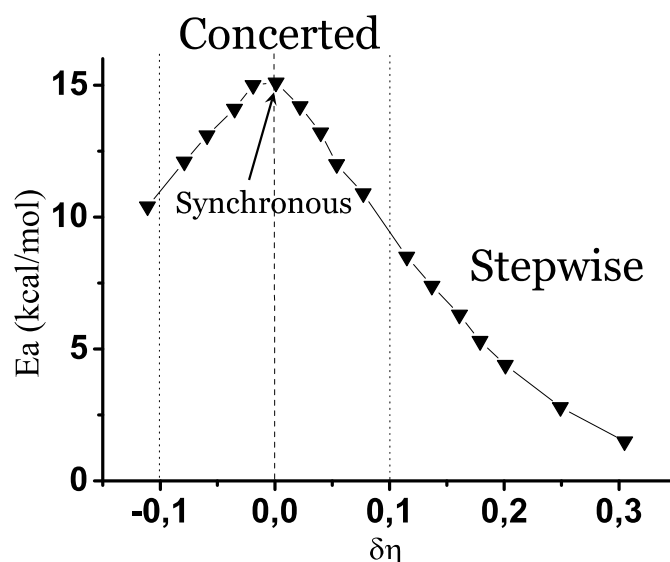


Figure 15. Variation of $\delta\eta$ in function of δE_2 .

Variation of $\delta\eta$ as a function of the reaction barrier height is displayed in Figure 16. The highest barrier height was found for the $\delta\eta \cong 0$, where both proton transfers are being simultaneously carried out. Elsewhere ($\delta\eta \neq 0$), the two protons are transferred either by the asynchronous concerted mechanism ($|\delta\eta| < 0.1$) or by the step-by-step mechanism ($\delta\eta > 0.1$), i.e. one proton at a time.

Figure 16. Variation of barrier height in function of $\delta\eta$.

Accordingly, the difference between two ELF bifurcations at hydrogen bonds, $\delta\eta$, calculated on the reactant structure formed at the entrance channel, not only provides a good indicator for the H-bond strength, but also allows us to predict the evolution of the system during the proton transfer reaction.

III. Conclusions

To summarize, in this work, we provide some insight on the nature of double proton transfer reaction between pyrazole and guanidine presenting a peculiar plateau in the transition state region. Free-field pyrazole–guanidine is actually a strongly asynchronous concerted reaction. Application of an oriented external electric field could allow the system changes either from the concerted to stepwise mechanism, or from an asynchronous process to a perfect synchronous double proton transfer reaction.

On the basis of the analysis presented in this paper, we want to draw the following conclusions:

- i. In the case of free-field pyrazole–guanidine system, topological analysis reveals that the “plateau transition region”, although energetically degenerated, hosts two remarkable changes of the monosynaptic valence basins, characterising the non-bonding electron density

on the N atom (the lone pair), that mark the end of the proton transfer in the reverse direction, and the beginning of the second proton transfer in the forward direction. Rearrangement of the topological population clearly evidenced that the first proton transfer occurs on the rising flank of the energetic profile from pyrazole to guanidine, and the second proton transfer on the falling flank in the opposite direction.

- ii. The electronic reorganization and polarization along the N–H···N proton transfer bond axis cause an increase of the non-bonding electron density of the proton acceptor atom and a lengthening of the N–H distance of the corresponding proton donor when the applied electric field is oriented in the opposite direction of proton transfer bond axis.
- iii. Thanks to the polarization of the (N–H)_{pyrazole}···N_{guanidine} the V(N–H) basin population exceeds 3 e, making thus the N–H bond breaking feasible, when the complex is exposed to a negative electric field ($F_z < 0$). However, a reaction intermediate is formed along the pathway corresponding to a step-wise mechanism (a single proton transfer). It is worth to note that the energetic barrier height corresponding to the pyrazole–guanidine → pyrazolate–guanidinium reaction decreases when the electric field becomes more and more negative.
- iv. Application of a positive electric field ($F_z > 0$) to the pyrazole–guanidine complex reduces the plateau width and increases the barrier height. At $F_z = 40 \times 10^{-4}$ au, the double proton transfer occurs within a synchronous mechanism with the highest barrier height. The transition structure is then composed of three fragments: two wandering dressed protons in sandwich between a deprotonated pyrazole and a deprotonated guanidine. The barrier height decreases and the plateau appears again when $40 \times 10^{-4} < F_z \leq 80 \times 10^{-4}$ au with reversal of the order in which both protons are transferred.
- v. It has been shown that the ELF value at the saddle point linking the proton donor to the proton acceptor domains in the reactant complex reflects well the variation of the hydrogen bond strength. Especially, the difference between two ELF values at the two hydrogen bonds could be used as a clear-cut descriptor to estimate the synchronicity and also the variation of the barrier height during the double proton transfer reaction.

Supporting Information

Remarkable points on the energy profile and evolution of distances along the reaction path, snapshots of some key ELF basins on the plateau transition state and their population, PCA portion of variance, cumulative portion of variance expressed by each principal component, atomic motion on PC1 and PC2 for five remarkable points and PCA details on the transition state region, averaged trajectory by BOMD

1
2
3 calculation over four trajectories, full potential energy profile of DPT in pyrazole-guanidine for OEEF in
4 negative direction of 60×10^{-4} au intensity, geometries Cartesian coordinates.
5
6
7
8
9
10
11
12
13
14
15
16
17
18
19
20
21
22
23
24
25
26
27
28
29
30
31
32
33
34
35
36
37
38
39
40
41
42
43
44
45
46
47
48
49
50
51
52
53
54
55
56
57
58
59
60

References

- (1) Rozas, I.; Alkorta, I.; Elguero, J. Field Effects on Dihydrogen Bonded Systems. *Chem. Phys. Lett.* **1997**, *275* (3–4), 423–428. [https://doi.org/10.1016/S0009-2614\(97\)00767-7](https://doi.org/10.1016/S0009-2614(97)00767-7).
- (2) Ramos, M.; Alkorta, I.; Elguero, J.; Golubev, N. S.; Denisov, G. S.; Benedict, H.; Limbach, H.-H. Theoretical Study of the Influence of Electric Fields on Hydrogen-Bonded Acid–Base Complexes. *J. Phys. Chem. A* **1997**, *101* (50), 9791–9800. <https://doi.org/10.1021/jp972586q>.
- (3) Shenderovich, I. G.; Denisov, G. S. Modeling of Solute-Solvent Interactions Using an External Electric Field—From Tautomeric Equilibrium in Nonpolar Solvents to the Dissociation of Alkali Metal Halides. *Molecules* **2021**, *26* (5), 1283. <https://doi.org/10.3390/molecules26051283>.
- (4) Scheiner, S.; Redfern, P.; Szczesniak, M. M. Effects of External Ions on the Energetics of Proton Transfers across Hydrogen Bonds. *J. Phys. Chem.* **1985**, *89* (2), 262–266. <https://doi.org/10.1021/j100248a017>.
- (5) Boda, M.; Naresh Patwari, G. Insights into Acid Dissociation of HCl and HBr with Internal Electric Fields. *Phys. Chem. Chem. Phys.* **2017**, *19* (11), 7461–7464. <https://doi.org/10.1039/C6CP08870H>.
- (6) Persson, B. N. J.; Avouris, Ph. The Effects of the Electric Field in the STM on Excitation Localization. Implications for Local Bond Breaking. *Chem. Phys. Lett.* **1995**, *242* (4–5), 483–489. [https://doi.org/10.1016/0009-2614\(95\)00778-3](https://doi.org/10.1016/0009-2614(95)00778-3).
- (7) Shenderovich, I. G. Electric Field Effect on ^{31}P NMR Magnetic Shielding. *J. Chem. Phys.* **2020**, *153* (18), 184501. <https://doi.org/10.1063/5.0031167>.
- (8) Shenderovich, I. G.; Denisov, G. S. Modeling of the Response of Hydrogen Bond Properties on an External Electric Field: Geometry, NMR Chemical Shift, Spin-Spin Scalar Coupling. *Molecules* **2021**, *26* (16), 4967. <https://doi.org/10.3390/molecules26164967>.
- (9) Jordan, M. J. T.; Del Bene, J. E. Unraveling Environmental Effects on Hydrogen-Bonded Complexes: Matrix Effects on the Structures and Proton-Stretching Frequencies of Hydrogen–Halide Complexes with Ammonia and Trimethylamine. *J. Am. Chem. Soc.* **2000**, *122* (9), 2101–2115. <https://doi.org/10.1021/ja993981s>.
- (10) Mollica Nardo, V.; Cassone, G.; Ponterio, R. C.; Saija, F.; Sponer, J.; Tommasini, M.; Trusso, S. Electric-Field-Induced Effects on the Dipole Moment and Vibrational Modes of the Centrosymmetric Indigo Molecule. *J. Phys. Chem. A* **2020**, *124* (51), 10856–10869. <https://doi.org/10.1021/acs.jpca.0c09791>.
- (11) Geppert, S.; Rabold, A.; Zundel, G.; Eckert, M. Theoretical Treatment of Spectroscopic Data for a Strong Hydrogen Bond with a Broad Single-Minimum Proton Potential. *J. Phys. Chem.* **1995**, *99* (32), 12220–12224. <https://doi.org/10.1021/j100032a026>.
- (12) Sowlati-Hashjin, S.; Matta, C. F. The Chemical Bond in External Electric Fields: Energies, Geometries, and Vibrational Stark Shifts of Diatomic Molecules. *J. Chem. Phys.* **2013**, *139* (14), 144101. <https://doi.org/10.1063/1.4820487>.

- 1
2
3 (13) Giribet, C. G.; Vizioli, C. V.; de Azúa, M. C. R.; Contreras, R. H.; Dannenberg, J. J.; Masunov, A.
4 Proximity Effects on Nuclear Spin–Spin Coupling Constants. Part 2.—The Electric Field Effect on $^1\text{J}(\text{CH})$
5 Couplings. *J Chem Soc Faraday Trans* **1996**, *92* (17), 3029–3033.
6 <https://doi.org/10.1039/FT9969203029>.
7
8
9 (14) Chen, L.; Dang, J.; Du, J.; Wang, C.; Mo, Y. Hydrogen and Halogen Bonding in Homogeneous External
10 Electric Fields: Modulating the Bond Strengths. *Chem. – Eur. J.* **2021**, *27* (56), 14042–14050.
11 <https://doi.org/10.1002/chem.202102284>.
12
13 (15) Foroutan-Nejad, C.; Marek, R. Potential Energy Surface and Binding Energy in the Presence of an
14 External Electric Field: Modulation of Anion– π Interactions for Graphene-Based Receptors. *Phys Chem*
15 *Chem Phys* **2014**, *16* (6), 2508–2514. <https://doi.org/10.1039/C3CP52671B>.
16
17 (16) Masunov, A.; Dannenberg, J. J.; Contreras, R. H. C–H Bond-Shortening upon Hydrogen Bond
18 Formation: Influence of an Electric Field. *J. Phys. Chem. A* **2001**, *105* (19), 4737–4740.
19 <https://doi.org/10.1021/jp0043470>.
20
21 (17) Golubev, N. S.; Shenderovich, I. G.; Smirnov, S. N.; Denisov, G. S.; Limbach, H.-H. Nuclear Scalar Spin-
22 Spin Coupling Reveals Novel Properties of Low-Barrier Hydrogen Bonds in a Polar Environment. *Chem.*
23 *- Eur. J.* **1999**, *5* (2), 492–497. [https://doi.org/10.1002/\(SICI\)1521-3765\(19990201\)5:2<492::AID-](https://doi.org/10.1002/(SICI)1521-3765(19990201)5:2<492::AID-CHEM492>3.0.CO;2-I)
24 [CHEM492>3.0.CO;2-I](https://doi.org/10.1002/(SICI)1521-3765(19990201)5:2<492::AID-CHEM492>3.0.CO;2-I).
25
26 (18) Mata, I.; Alkorta, I.; Espinosa, E.; Molins, E. Relationships between Interaction Energy, Intermolecular
27 Distance and Electron Density Properties in Hydrogen Bonded Complexes under External Electric
28 Fields. *Chem. Phys. Lett.* **2011**, *507* (1–3), 185–189. <https://doi.org/10.1016/j.cplett.2011.03.055>.
29
30 (19) Mata, I.; Molins, E.; Alkorta, I.; Espinosa, E. Effect of an External Electric Field on the Dissociation
31 Energy and the Electron Density Properties: The Case of the Hydrogen Bonded Dimer $\text{HF}\cdots\text{HF}$. *J.*
32 *Chem. Phys.* **2009**, *130* (4), 044104. <https://doi.org/10.1063/1.3065972>.
33
34 (20) Dannenberg, J. J.; Haskamp, L.; Masunov, A. Are Hydrogen Bonds Covalent or Electrostatic? A
35 Molecular Orbital Comparison of Molecules in Electric Fields and H-Bonding Environments. *J. Phys.*
36 *Chem. A* **1999**, *103* (35), 7083–7086. <https://doi.org/10.1021/jp991010t>.
37
38 (21) Bouteiller, Y.; Sadi, S.; Latajka, Z.; Ratajczak, H. Ab Initio Study of Proton Transfer between
39 Methylnitroamine and Trimethylamine. *Chem. Phys. Lett.* **1992**, *199* (1–2), 55–61.
40 [https://doi.org/10.1016/0009-2614\(92\)80048-G](https://doi.org/10.1016/0009-2614(92)80048-G).
41
42 (22) Gheorghiu, A.; Coveney, P. V.; Arabi, A. A. The Influence of External Electric Fields on Proton Transfer
43 Tautomerism in the Guanine–Cytosine Base Pair. *Phys. Chem. Chem. Phys.* **2021**,
44 [10.1039.D0CP06218A](https://doi.org/10.1039/D0CP06218A). <https://doi.org/10.1039/D0CP06218A>.
45
46 (23) Zhou, Z.-J.; Li, X.-P.; Liu, Z.-B.; Li, Z.-R.; Huang, X.-R.; Sun, C.-C. Electric Field-Driven Acid–Base
47 Chemistry: Proton Transfer from Acid (HCl) to Base ($\text{NH}_3/\text{H}_2\text{O}$). *J. Phys. Chem. A* **2011**, *115* (8),
48 1418–1422. <https://doi.org/10.1021/jp110408y>.
49
50 (24) Warshel, A.; Sharma, P. K.; Kato, M.; Xiang, Y.; Liu, H.; Olsson, M. H. M. Electrostatic Basis for Enzyme
51 Catalysis. *Chem. Rev.* **2006**, *106* (8), 3210–3235. <https://doi.org/10.1021/cr0503106>.
52
53
54
55
56
57
58
59
60

- 1
2
3 (25) Warshel, A. Electrostatic Origin of the Catalytic Power of Enzymes and the Role of Preorganized Active
4 Sites. *J. Biol. Chem.* **1998**, *273* (42), 27035–27038. <https://doi.org/10.1074/jbc.273.42.27035>.
5
6 (26) Wu, Y.; Boxer, S. G. A Critical Test of the Electrostatic Contribution to Catalysis with Noncanonical
7 Amino Acids in Ketosteroid Isomerase. *J. Am. Chem. Soc.* **2016**, *138* (36), 11890–11895.
8 <https://doi.org/10.1021/jacs.6b06843>.
9
10 (27) Schneider, S. H.; Boxer, S. G. Vibrational Stark Effects of Carbonyl Probes Applied to Reinterpret IR
11 and Raman Data for Enzyme Inhibitors in Terms of Electric Fields at the Active Site. *J. Phys. Chem. B*
12 **2016**, *120* (36), 9672–9684. <https://doi.org/10.1021/acs.jpcc.6b08133>.
13
14 (28) Wu, Y.; Fried, S. D.; Boxer, S. G. A Preorganized Electric Field Leads to Minimal Geometrical
15 Reorientation in the Catalytic Reaction of Ketosteroid Isomerase. *J. Am. Chem. Soc.* **2020**, *142* (22),
16 9993–9998. <https://doi.org/10.1021/jacs.0c00383>.
17
18 (29) Wang, X.; He, X. An Ab Initio QM/MM Study of the Electrostatic Contribution to Catalysis in the Active
19 Site of Ketosteroid Isomerase. *Molecules* **2018**, *23* (10), 2410.
20 <https://doi.org/10.3390/molecules23102410>.
21
22 (30) Hennefarth, M. R.; Alexandrova, A. N. Advances in Optimizing Enzyme Electrostatic Preorganization.
23 *Curr. Opin. Struct. Biol.* **2022**, *72*, 1–8. <https://doi.org/10.1016/j.sbi.2021.06.006>.
24
25 (31) Vaissier, V.; Sharma, S. C.; Schaettle, K.; Zhang, T.; Head-Gordon, T. Computational Optimization of
26 Electric Fields for Improving Catalysis of a Designed Kemp Eliminase. *ACS Catal.* **2018**, *8* (1), 219–227.
27 <https://doi.org/10.1021/acscatal.7b03151>.
28
29 (32) Welborn, V. V.; Ruiz Pestana, L.; Head-Gordon, T. Computational Optimization of Electric Fields for
30 Better Catalysis Design. *Nat. Catal.* **2018**, *1* (9), 649–655. <https://doi.org/10.1038/s41929-018-0109-2>.
31
32 (33) Aragonès, A. C.; Haworth, N. L.; Darwish, N.; Ciampi, S.; Bloomfield, N. J.; Wallace, G. G.; Díez-Pérez, I.;
33 Coote, M. L. Electrostatic Catalysis of a Diels–Alder Reaction. *Nature* **2016**, *531* (7592), 88–91.
34 <https://doi.org/10.1038/nature16989>.
35
36 (34) Shaik, S.; Mandal, D.; Ramanan, R. Oriented Electric Fields as Future Smart Reagents in Chemistry.
37 *Nat. Chem.* **2016**, *8*, 1091–1098. <https://doi.org/10.1038/nchem.2651>.
38
39 (35) Léonard, N. G.; Dhaoui, R.; Chantarojsiri, T.; Yang, J. Y. Electric Fields in Catalysis: From Enzymes to
40 Molecular Catalysts. *ACS Catal.* **2021**, *11* (17), 10923–10932.
41 <https://doi.org/10.1021/acscatal.1c02084>.
42
43 (36) Ciampi, S.; Darwish, N.; Aitken, H. M.; Díez-Pérez, I.; Coote, M. L. Harnessing Electrostatic Catalysis in
44 Single Molecule, Electrochemical and Chemical Systems: A Rapidly Growing Experimental Tool Box.
45 *Chem. Soc. Rev.* **2018**, *47* (14), 5146–5164. <https://doi.org/10.1039/C8CS00352A>.
46
47 (37) Shaik, S.; Danovich, D.; Joy, J.; Wang, Z.; Stuyver, T. Electric-Field Mediated Chemistry: Uncovering
48 and Exploiting the Potential of (Oriented) Electric Fields to Exert Chemical Catalysis and Reaction
49 Control. *J. Am. Chem. Soc.* **2020**, *142* (29), 12551–12562. <https://doi.org/10.1021/jacs.0c05128>.
50
51
52
53
54
55
56
57
58
59
60

- 1
2
3 (38) Che, F.; Gray, J. T.; Ha, S.; Kruse, N.; Scott, S. L.; McEwen, J.-S. Elucidating the Roles of Electric Fields in
4 Catalysis: A Perspective. *ACS Catal.* **2018**, *8* (6), 5153–5174.
5 <https://doi.org/10.1021/acscatal.7b02899>.
6
7
8 (39) Shaik, S.; de Visser, S. P.; Kumar, D. External Electric Field Will Control the Selectivity of Enzymatic-Like
9 Bond Activations. *J. Am. Chem. Soc.* **2004**, *126* (37), 11746–11749.
10 <https://doi.org/10.1021/ja047432k>.
11
12 (40) Meir, R.; Chen, H.; Shaik, S. Oriented Electric Fields Accelerate Diels–Alder Reactions and Control the
13 Endo/Exo Selectivity. *ChemPhysChem* **2010**, *11* (1), 301–310.
14 <https://doi.org/10.1002/cphc.200900848>.
15
16
17 (41) Shaik, S.; Shurki, A. Valence Bond Diagrams and Chemical Reactivity. *Angew. Chem. Int. Ed.* **1999**, *38*
18 (5), 586–625. [https://doi.org/10.1002/\(SICI\)1521-3773\(19990301\)38:5<586::AID-ANIE586>3.0.CO;2-T](https://doi.org/10.1002/(SICI)1521-3773(19990301)38:5<586::AID-ANIE586>3.0.CO;2-T).
19
20 (42) Usharani, D.; Lai, W.; Li, C.; Chen, H.; Danovich, D.; Shaik, S. A Tutorial for Understanding Chemical
21 Reactivity through the Valence Bond Approach. *Chem Soc Rev* **2014**, *43* (14), 4968–4988.
22 <https://doi.org/10.1039/C4CS00043A>.
23
24 (43) Stuyver, T.; Danovich, D.; Joy, J.; Shaik, S. External Electric Field Effects on Chemical Structure and
25 Reactivity. *WIREs Comput. Mol. Sci.* **2020**, *10* (2). <https://doi.org/10.1002/wcms.1438>.
26
27 (44) Shaik, S.; Ramanan, R.; Danovich, D.; Mandal, D. Structure and Reactivity/Selectivity Control by
28 Oriented-External Electric Fields. *Chem. Soc. Rev.* **2018**, *47* (14), 5125–5145.
29 <https://doi.org/10.1039/C8CS00354H>.
30
31 (45) Wang, Z.; Danovitch, D.; Ramanan, R.; Shaik, S. Oriented-External Electric Fields Create Absolute
32 Enantioselectivity in Diels–Alder Reactions: Importance of the Molecular Dipole Moment. *J. Am.*
33 *Chem. Soc.* **2018**, *140* (41), 13350–13359. <https://doi.org/10.1021/jacs.8b08233>.
34
35 (46) *Effects of Electric Fields on Structure and Reactivity: New Horizons in Chemistry*; Shaik, S., Stuyver, T.,
36 Eds.; Theoretical and Computational Chemistry Series; Royal Society of Chemistry: Cambridge, 2021.
37 <https://doi.org/10.1039/9781839163043>.
38
39 (47) Stuyver, T.; Danovitch, D.; De Proft, F.; Shaik, S. Electrophilic Aromatic Substitution Reactions:
40 Mechanistic Landscape, Electrostatic and Electric-Field Control of Reaction Rates and Mechanistic
41 Crossovers. *J. Am. Chem. Soc.* **2019**, *141* (24), 9719–9730. <https://doi.org/10.1021/jacs.9b04982>.
42
43 (48) Ramanan, R.; Danovich, D.; Mandal, D.; Shaik, S. Catalysis of Methyl Transfer Reactions by Oriented
44 External Electric Fields: Are Gold–Thiolate Linkers Innocent? *J. Am. Chem. Soc.* **2018**, *140* (12), 4354–
45 4362. <https://doi.org/10.1021/jacs.8b00192>.
46
47 (49) Seminario, J. M.; Concha, M. C.; Politzer, P. Calculated Structures and Relative Stabilities of Furoxan,
48 Some 1,2-Dinitrosoethylenes and Other Isomers. *J. Comput. Chem.* **1992**, *13* (2), 177–182.
49 <https://doi.org/10.1002/jcc.540130209>.
50
51 (50) Stevens, J.; Schweizer, M.; Rauhut, G. Toward an Understanding of the Furoxan–Dinitrosoethylene
52 Equilibrium. *J. Am. Chem. Soc.* **2001**, *123* (30), 7326–7333. <https://doi.org/10.1021/ja010792c>.
53
54
55
56
57
58
59
60

- 1
2
3 (51) Schweiger, S.; Rauhut, G. Plateau Reactions: Double Proton-Transfer Processes with Structureless
4 Transition States. *J. Phys. Chem. A* **2003**, *107* (45), 9668–9678. <https://doi.org/10.1021/jp0350060>.
5
6 (52) Schweiger, S.; Hartke, B.; Rauhut, G. Double Proton Transfer Reactions at the Transition from a
7 Concerted to a Stepwise Mechanism: A Comparative Ab Initio Study. *Phys. Chem. Chem. Phys.* **2005**, *7*
8 (3), 493. <https://doi.org/10.1039/b415528a>.
9
10 (53) Schweiger, S.; Hartke, B.; Rauhut, G. Analysis and Dynamics of Unusual Double Proton Transfer
11 Reactions Based on the Reaction Path Hamiltonian. *Phys. Chem. Chem. Phys.* **2004**, *6* (13), 3341.
12 <https://doi.org/10.1039/b402534b>.
13
14 (54) Schweiger, S.; Rauhut, G. Double Proton Transfer Reactions with Plateau-Like Transition State
15 Regions: Pyrazole–Trifluoroacetic Acid Clusters. *J. Phys. Chem. A* **2006**, *110* (8), 2816–2820.
16 <https://doi.org/10.1021/jp0569842>.
17
18 (55) von Horsten, H. F.; Rauhut, G.; Hartke, B. Fingerprints of Delocalized Transition States in Quantum
19 Dynamics. *J. Phys. Chem. A* **2006**, *110* (48), 13014–13021. <https://doi.org/10.1021/jp063051c>.
20
21 (56) von Horsten, H. F.; Hartke, B. Links between Potential Energy Structures and Quantum Cumulative
22 Reaction Probabilities of Double Proton Transfer Reactions. *Chem. Phys.* **2007**, *338* (2–3), 160–167.
23 <https://doi.org/10.1016/j.chemphys.2007.03.011>.
24
25 (57) Arabi, A. A.; Matta, C. F. Effects of Intense Electric Fields on the Double Proton Transfer in the
26 Watson–Crick Guanine–Cytosine Base Pair. *J. Phys. Chem. B* **2018**, *122* (37), 8631–8641.
27 <https://doi.org/10.1021/acs.jpcc.8b05053>.
28
29 (58) Lim, J.-H.; Lee, E. K.; Kim, Y. Theoretical Study for Solvent Effect on the Potential Energy Surface for
30 the Double Proton Transfer in Formic Acid Dimer and Formamidinium Dimer. *J. Phys. Chem. A* **1997**, *101*
31 (12), 2233–2239. <https://doi.org/10.1021/jp9626226>.
32
33 (59) Frisch, M. J.; Trucks, G. W.; Cheeseman, J. R.; Scalmani, G.; Caricato, M.; Hratchian, H. P.; Li, X.;
34 Barone, V.; Bloino, J.; Zheng, G.; Vreven, T.; Montgomery, J. A.; Petersson, G. A.; Scuseria, G. E.;
35 Schlegel, H. B.; Nakatsuji, H.; Izmaylov, A. F.; Martin, R. L.; Sonnenberg, J. L.; Peralta, J. E.; Heyd, J. J.;
36 Brothers, E.; Ogliaro, F.; Bearpark, M.; Robb, M. A.; Mennucci, B.; Kudin, K. N.; Staroverov, V. N.;
37 Kobayashi, R.; Normand, J.; Rendell, A.; Gomperts, R.; Zakrzewski, V. G.; Hada, M.; Ehara, M.; Toyota,
38 K.; Fukuda, R.; Hasegawa, J.; Ishida, M.; Nakajima, T.; Honda, Y.; Kitao, O.; Nakai, H. *Gaussian 09*;
39 Gaussian, Inc.: Wallingford CT, 2013.
40
41 (60) Körzdörfer, T.; Sears, J. S.; Sutton, C.; Brédas, J.-L. Long-Range Corrected Hybrid Functionals for π -
42 Conjugated Systems: Dependence of the Range-Separation Parameter on Conjugation Length. *J.*
43 *Chem. Phys.* **2011**, *135* (20), 204107. <https://doi.org/10.1063/1.3663856>.
44
45 (61) Chai, J.-D.; Head-Gordon, M. Systematic Optimization of Long-Range Corrected Hybrid Density
46 Functionals. *J. Chem. Phys.* **2008**, *128* (8), 084106. <https://doi.org/10.1063/1.2834918>.
47
48 (62) Krishnan, R.; Binkley, J. S.; Seeger, R.; Pople, J. A. Self-consistent Molecular Orbital Methods. XX. A
49 Basis Set for Correlated Wave Functions. *J. Chem. Phys.* **1980**, *72* (1), 650–654.
50 <https://doi.org/10.1063/1.438955>.
51
52
53
54
55
56
57
58
59
60

- 1
2
3 (63) McLean, A. D.; Chandler, G. S. Contracted Gaussian Basis Sets for Molecular Calculations. I. Second
4 Row Atoms, $Z=11-18$. *J. Chem. Phys.* **1980**, *72* (10), 5639–5648. <https://doi.org/10.1063/1.438980>.
5
6
7 (64) Fukui, K. Formulation of the Reaction Coordinate. *J. Phys. Chem.* **1970**, *74* (23), 4161–4163.
8 <https://doi.org/10.1021/j100717a029>.
9
10 (65) Page, M.; McIver, J. W. On Evaluating the Reaction Path Hamiltonian. *J. Chem. Phys.* **1988**, *88* (2),
11 922–935. <https://doi.org/10.1063/1.454172>.
12
13 (66) Page, M.; Doubleday, C.; McIver, J. W. Following Steepest Descent Reaction Paths. The Use of Higher
14 Energy Derivatives with *ab initio* Electronic Structure Methods. *J. Chem. Phys.* **1990**, *93* (8), 5634–
15 5642. <https://doi.org/10.1063/1.459634>.
16
17
18 (67) Yepes, D.; Munarriz, J.; Daniel l’Anson; Contreras-Garcia, J.; Jaque, P. Real-Space Approach to the
19 Reaction Force: Understanding the Origin of Synchronicity/Nonsynchronicity in Multibond Chemical
20 Reactions. *J. Phys. Chem. A* **2020**, *124* (10), 1959–1972. <https://doi.org/10.1021/acs.jpca.9b10508>.
21
22
23 (68) Yepes, D.; Donoso-Tauda, O.; Pérez, P.; Murray, J. S.; Politzer, P.; Jaque, P. The Reaction Force
24 Constant as an Indicator of Synchronicity/Nonsynchronicity in [4+2] Cycloaddition Processes. *Phys.*
25 *Chem. Chem. Phys.* **2013**, *15* (19), 7311. <https://doi.org/10.1039/c3cp44197k>.
26
27
28 (69) Jaque, P.; Toro-Labbé, A.; Politzer, P.; Geerlings, P. Reaction Force Constant and Projected Force
29 Constants of Vibrational Modes along the Path of an Intramolecular Proton Transfer Reaction. *Chem.*
30 *Phys. Lett.* **2008**, *456* (4–6), 135–140. <https://doi.org/10.1016/j.cplett.2008.03.054>.
31
32
33 (70) Jaque, P.; Toro-Labbé, A. Theoretical Study of the Double Proton Transfer in the CHX–XH...CHX–XH (X
34 = O, S) Complexes. *J. Phys. Chem. A* **2000**, *104* (5), 995–1003. <https://doi.org/10.1021/jp993016o>.
35
36
37 (71) Toro-Labbé, A. Characterization of Chemical Reactions from the Profiles of Energy, Chemical
38 Potential, and Hardness. *J. Phys. Chem. A* **1999**, *103* (22), 4398–4403.
39 <https://doi.org/10.1021/jp984187g>.
40
41
42 (72) Labet, V.; Morell, C.; Toro-Labbé, A.; Grand, A. Is an Elementary Reaction Step Really Elementary?
43 Theoretical Decomposition of Asynchronous Concerted Mechanisms. *Phys. Chem. Chem. Phys.* **2010**,
44 *12* (16), 4142. <https://doi.org/10.1039/b924589h>.
45
46
47 (73) Weinhold, F.; Landis, C. R. NATURAL BOND ORBITALS AND EXTENSIONS OF LOCALIZED BONDING
48 CONCEPTS. *Chem Educ Res Pr.* **2001**, *2* (2), 91–104. <https://doi.org/10.1039/B1RP90011K>.
49
50
51 (74) Weinhold, F.; Klein, R. A. What Is a Hydrogen Bond? Mutually Consistent Theoretical and
52 Experimental Criteria for Characterizing H-Bonding Interactions. *Mol. Phys.* **2012**, *110* (9–10), 565–
53 579. <https://doi.org/10.1080/00268976.2012.661478>.
54
55
56 (75) Weinhold, F.; Klein, R. A. What Is a Hydrogen Bond? Resonance Covalency in the Supramolecular
57 Domain. *Chem Educ Res Pr.* **2014**, *15* (3), 276–285. <https://doi.org/10.1039/C4RP00030G>.
58
59
60

- 1
2
3 (76) Weinhold, F.; Landis, C. R. *Discovering Chemistry with Natural Bond Orbitals: Weinhold/Discovering*
4 *Chemistry*; John Wiley & Sons, Inc.: Hoboken, NJ, USA, 2012.
5 <https://doi.org/10.1002/9781118229101>.
6
7
8 (77) Becke, A. D.; Edgecombe, K. E. A Simple Measure of Electron Localization in Atomic and Molecular
9 Systems. *J. Chem. Phys.* **1990**, *92* (9), 5397–5403. <https://doi.org/10.1063/1.458517>.
10
11 (78) Silvi, B.; Savin, A. Classification of Chemical Bonds Based on Topological Analysis of Electron
12 Localization Functions. *Nature* **1994**, *371* (6499), 683–686. <https://doi.org/10.1038/371683a0>.
13
14 (79) Grin, Y.; Savin, A.; Silvi, B. The ELF Perspective of Chemical Bonding. In *The Chemical Bond*; Frenking,
15 G., Shaik, S., Eds.; Wiley-VCH Verlag GmbH & Co. KGaA: Weinheim, Germany, 2014; pp 345–382.
16 <https://doi.org/10.1002/9783527664696.ch10>.
17
18 (80) Alikhani, M. E.; Bouteiller, Y.; Silvi, B. Bonding, Electronic, and Vibrational Analysis of the Al–C₂H₄
19 Complex Using Density Functional Theory and Topological Method (ELF). *J. Phys. Chem.* **1996**, *100*
20 (40), 16092–16097. <https://doi.org/10.1021/jp9535351>.
21
22 (81) Alikhani, M. E.; Fuster, F.; Silvi, B. What Can Tell the Topological Analysis of ELF on Hydrogen Bonding?
23 *Struct. Chem.* **2005**, *16* (3), 203–210. <https://doi.org/10.1007/s11224-005-4451-z>.
24
25 (82) Silvi, B.; Fourré, I.; Alikhani, M. E. The Topological Analysis of the Electron Localization Function. A Key
26 for a Position Space Representation of Chemical Bonds. *Monatshefte Für Chem. - Chem. Mon.* **2005**,
27 *136* (6), 855–879. <https://doi.org/10.1007/s00706-005-0297-8>.
28
29 (83) Zins, E.-L.; Silvi, B.; Alikhani, M. E. Activation of C–H and B–H Bonds through Agostic Bonding: An
30 ELF/QTAIM Insight. *Phys. Chem. Chem. Phys.* **2015**, *17* (14), 9258–9281.
31 <https://doi.org/10.1039/C4CP05728G>.
32
33 (84) Alikhani, M. E. On the Chemical Bonding Features in Boron Containing Compounds: A Combined
34 QTAIM/ELF Topological Analysis. *Phys. Chem. Chem. Phys.* **2013**, *15* (30), 12602.
35 <https://doi.org/10.1039/c3cp50396h>.
36
37 (85) Michelini, M. D. C.; Russo, N.; Alikhani, M. E.; Silvi, B. Energetic and Topological Analysis of the
38 Reaction of Mo and Mo₂ with NH₃, C₂H₂, and C₂H₄ Molecules. *J. Comput. Chem.* **2004**, *25* (13),
39 1647–1655. <https://doi.org/10.1002/jcc.20087>.
40
41 (86) Noury, S.; Silvi, B.; Gillespie, R. J. Chemical Bonding in Hypervalent Molecules: Is the Octet Rule
42 Relevant? *Inorg. Chem.* **2002**, *41* (8), 2164–2172. <https://doi.org/10.1021/ic011003v>.
43
44 (87) Berski, S.; Gordon, A. J.; Latajka, Z. Electron Localization Function Study on the Chemical Bonding in a
45 Real Space for Tetrahedrane, Cubane, Adamantane, and Dodecahedrane and Their Perfluorinated
46 Derivatives and Radical Anions. *J. Phys. Chem. A* **2014**, *118* (23), 4147–4156.
47 <https://doi.org/10.1021/jp501838g>.
48
49 (88) Martín Pendás, A.; Francisco, E.; Blanco, M. A. Electron–Electron Interactions between ELF Basins.
50 *Chem. Phys. Lett.* **2008**, *454* (4–6), 396–403. <https://doi.org/10.1016/j.cplett.2008.02.029>.
51
52
53
54
55
56
57
58
59
60

- 1
2
3 (89) Gillespie, R. J. Fifty Years of the VSEPR Model. *Coord. Chem. Rev.* **2008**, *252* (12–14), 1315–1327.
4 <https://doi.org/10.1016/j.ccr.2007.07.007>.
5
6 (90) Gillespie, R. J.; Noury, S.; Pilmé, J.; Silvi, B. An Electron Localization Function Study of the Geometry of
7 d^0 Molecules of the Period 4 Metals Ca to Mn. *Inorg. Chem.* **2004**, *43* (10), 3248–3256.
8 <https://doi.org/10.1021/ic0354015>.
9
10 (91) Steinmann, S. N.; Mo, Y.; Corminboeuf, C. How Do Electron Localization Functions Describe π -Electron
11 Delocalization? *Phys. Chem. Chem. Phys.* **2011**, *13* (46), 20584. <https://doi.org/10.1039/c1cp21055f>.
12
13 (92) Alikhani, E.; Fuster, F.; Madebene, B.; Grabowski, S. J. Topological Reaction Sites – Very Strong
14 Chalcogen Bonds. *Phys Chem Chem Phys* **2014**, *16* (6), 2430–2442.
15 <https://doi.org/10.1039/C3CP54208D>.
16
17 (93) *Applications of Topological Methods in Molecular Chemistry*; Chauvin, R., Lepetit, C., Silvi, B., Alikhani,
18 E., Eds.; Challenges and advances in computational chemistry and physics; Springer: Switzerland,
19 2016.
20
21 (94) Krokidis, X.; Silvi, B.; Alikhani, M. E. Topological Characterization of the Isomerization Mechanisms in
22 XNO (X=H, Cl). *Chem. Phys. Lett.* **1998**, *292* (1–2), 35–45. [https://doi.org/10.1016/S0009-](https://doi.org/10.1016/S0009-2614(98)00650-2)
23 [2614\(98\)00650-2](https://doi.org/10.1016/S0009-2614(98)00650-2).
24
25 (95) Berski, S.; Andrés, J.; Silvi, B.; Domingo, L. R. The Joint Use of Catastrophe Theory and Electron
26 Localization Function to Characterize Molecular Mechanisms. A Density Functional Study of the
27 Diels–Alder Reaction between Ethylene and 1,3-Butadiene. *J. Phys. Chem. A* **2003**, *107* (31), 6014–
28 6024. <https://doi.org/10.1021/jp030272z>.
29
30 (96) Polo, V.; Andres, J.; Castillo, R.; Berski, S.; Silvi, B. Understanding the Molecular Mechanism of the 1,3-
31 Dipolar Cycloaddition between Fulminic Acid and Acetylene in Terms of the Electron Localization
32 Function and Catastrophe Theory. *Chem. - Eur. J.* **2004**, *10* (20), 5165–5172.
33 <https://doi.org/10.1002/chem.200400161>.
34
35 (97) Fuster, F.; Silvi, B. Determination of Protonation Sites in Bases from Topological Rules. *Chem. Phys.*
36 **2000**, *252* (3), 279–287. [https://doi.org/10.1016/S0301-0104\(99\)00320-1](https://doi.org/10.1016/S0301-0104(99)00320-1).
37
38 (98) Silvi, B.; Ratajczak, H. Hydrogen Bonding and Delocalization in the ELF Analysis Approach. *Phys. Chem.*
39 *Chem. Phys.* **2016**, *18* (39), 27442–27449. <https://doi.org/10.1039/C6CP05400E>.
40
41 (99) Esmail Alikhani, M.; Silvi, B. A Topological Analysis of the Proton Transfer in the HF– and HCl–(OH)–
42 Interactions. *J. Mol. Struct.* **2004**, *706* (1–3), 3–6. <https://doi.org/10.1016/j.molstruc.2004.02.052>.
43
44 (100) Fuster, F.; Silvi, B. Does the Topological Approach Characterize the Hydrogen Bond? *Theor. Chem. Acc.*
45 *Theory Comput. Model. Theor. Chim. Acta* **2000**, *104* (1), 13–21.
46 <https://doi.org/10.1007/s002149900100>.
47
48 (101) Noury, S.; Krokidis, X.; Fuster, F.; Silvi, B. Computational Tools for the Electron Localization Function
49 Topological Analysis. *Comput. Chem.* **1999**, *23* (6), 597–604.
50
51
52
53
54
55
56
57
58
59
60

- 1
2
3 (102) Lu, T.; Chen, F. Multiwfn: A Multifunctional Wavefunction Analyzer. *J. Comput. Chem.* **2012**, *33* (5),
4 580–592. <https://doi.org/10.1002/jcc.22885>.
5
6
7 (103) Tian, L.; Fei-Wu, C.; 北京科技大学化学与生物工程学院, 北京 100083, School of Chemical and
8 Biological Engineering, University of Science and Technology Beijing, Beijing 100083, P. R. China.
9 Meaning and Functional Form of the Electron Localization Function. *Acta Phys.-Chim. Sin.* **2011**, *27*
10 (12), 2786–2792. <https://doi.org/10.3866/PKU.WHXB20112786>.
11
12 (104) Santos, J. C.; Andres, J.; Aizman, A.; Fuentealba, P.; Polo, V. A Theoretical Study on the Reaction
13 Mechanism for the Bergman Cyclization from the Perspective of the Electron Localization Function
14 and Catastrophe Theory. *J. Phys. Chem. A* **2005**, *109* (16), 3687–3693.
15 <https://doi.org/10.1021/jp0441947>.
16
17 (105) Krokidis, X.; Vuilleumier, R.; Borgis, D.; Silvi, B. A Topological Analysis of the Proton Transfer in H_5O^+
18 $_2$. *Mol. Phys.* **1999**, *96* (2), 265–273. <https://doi.org/10.1080/00268979909482959>.
19
20 (106) Polo, V.; Gonzalez-Navarrete, P.; Silvi, B.; Andres, J. An Electron Localization Function and Catastrophe
21 Theory Analysis on the Molecular Mechanism of Gas-Phase Identity SN_2 Reactions. *Theor. Chem. Acc.*
22 **2008**, *120* (4–6), 341–349. <https://doi.org/10.1007/s00214-008-0427-6>.
23
24 (107) Ćmikiewicz, A.; Gordon, A. J.; Berski, S. Characterisation of the Reaction Mechanism between
25 Ammonia and Formaldehyde from the Topological Analysis of ELF and Catastrophe Theory
26 Perspective. *Struct. Chem.* **2018**, *29* (1), 243–255. <https://doi.org/10.1007/s11224-017-1024-x>.
27
28 (108) Krokidis, X.; Noury, S.; Silvi, B. Characterization of Elementary Chemical Processes by Catastrophe
29 Theory. *J. Phys. Chem. A* **1997**, *101* (39), 7277–7282. <https://doi.org/10.1021/jp9711508>.
30
31 (109) Andrés, J.; González-Navarrete, P.; Safont, V. S.; Silvi, B. Curly Arrows, Electron Flow, and Reaction
32 Mechanisms from the Perspective of the Bonding Evolution Theory. *Phys. Chem. Chem. Phys.* **2017**, *19*
33 (43), 29031–29046. <https://doi.org/10.1039/C7CP06108K>.
34
35 (110) Contreras-García, J.; Recio, J. M. Electron Delocalization and Bond Formation under the ELF
36 Framework. *Theor. Chem. Acc.* **2011**, *128* (4–6), 411–418. [https://doi.org/10.1007/s00214-010-0828-](https://doi.org/10.1007/s00214-010-0828-1)
37 [1](https://doi.org/10.1007/s00214-010-0828-1).
38
39 (111) Krokidis, X.; Goncalves, V.; Savin, A.; Silvi, B. How Malonaldehyde Bonds Change during Proton
40 Transfer. *J. Phys. Chem. A* **1998**, *102* (26), 5065–5073. <https://doi.org/10.1021/jp9734282>.
41
42 (112) Krokidis, X.; Silvi, B.; Dezarnaud-Dandine, C.; Sevin, A. Topological Study, Using a Coupled ELF and
43 Catastrophe Theory Technique, of Electron Transfer in the $Li+Cl_2$ System. *New J. Chem.* **1998**, *22* (12),
44 1341. <https://doi.org/10.1039/a801838c>.
45
46 (113) Hare, S. R.; Bratholm, L. A.; Glowacki, D. R.; Carpenter, B. K. Low Dimensional Representations along
47 Intrinsic Reaction Coordinates and Molecular Dynamics Trajectories Using Interatomic Distance
48 Matrices. *Chem. Sci.* **2019**, *10* (43), 9954–9968. <https://doi.org/10.1039/C9SC02742D>.
49
50 (114) Eckert, Michael.; Zundel, Georg. Proton Polarizability, Dipole Moment, and Proton Transitions of an
51 $AH...B$. *Dblharw. A-...H+B Proton-Transfer Hydrogen Bond as a Function of an External Electrical Field:*
52
53
54
55
56
57
58
59